Auxetic cementitious cellular composite (ACCC) PVDF-based energy harvester

Xie, Jinbao; Xu, Yading; Wan, Zhi; Ghaderiaram, Ali; Schlangen, Erik; Šavija, Branko

DOI
10.1016/j.enbuild.2023.113582

Publication date
2023

Document Version
Final published version

Published in
Energy and Buildings

Energy & Buildings 298 (2023) 113582

Contents lists available at ScienceDirect

Energy & Buildings

journal homepage: www.elsevier.com/locate/enb

Auxetic cementitious cellular composite (ACCC) PVDF-based energy harvester

Jinbao Xie, Yading Xu *, Zhi Wan, Ali Ghaderiaram, Erik Schlangen, Branko Šavija

Microlab, Faculty of Civil Engineering and Geosciences, Delft University of Technology, Delft 2628CN, the Netherlands

ARTICLE INFO

Keywords:
Energy harvesting
Auxetic cementitious cellular composites
PVDF
Piezoelectric model

ABSTRACT

The high deformation capacity of auxetic cementitious cellular composites (ACCCs) makes them promising for strain-based energy harvesting applications in infrastructure. In this study, a novel piezoelectric energy harvester (PEH) with ACCCs and surface-mounted PVDF film based on strain-induced piezoelectric mechanisms has been designed, fabricated, and experimentally tested. Furthermore, a numerical model for simulating the energy harvesting of ACCC-PVDF system undergoing repeated mechanical loading has been established and validated against the experimental data. The mechanical behavior of ACCCs was simulated by the concrete damage plasticity model during the preloading stage, which was converted to the second-elasticity model during cyclic loading stage. Based on the mechanical responses, analytical formulas for piezoelectric effects were developed to calculate the output voltage of the PVDF film. The output voltages of the ACCCs-PVDF system under different loading amplitudes and loading frequencies were assessed. The experimental results and models of the ACCCs-PVDF energy harvester lay a solid foundation for utilizing architected cementitious composites in energy harvesting applications to supply self-power electronics in infrastructure.

1. Introduction

Energy harvesting is a process by which the ambient energy is captured and converted into usable electrical energy for self-powered devices, such as small-sized, portable, low-power, and remote electronics that do not require replacement or maintenance. The most common energy harvesting materials and devices include piezoelectrics [1,2], thermoelectrics [3], photovoltaics [4], triboelectrics [5], electromagnetics [6], etc. Among them, piezoelectric energy harvesters are especially effective given that they produce a wide range of voltage and power density regardless of weather conditions. Furthermore, they are small and easy for installation and processing with a low price. Recently, use of energy-harvesting systems in civil structures has aroused great interest, as it could potentially power infrastructures (e.g., buildings, railways, highways, bridges) with energy self-sufficiency. Civil structures are generally subjected to a wide range of reciprocating dynamic loads from railway, vehicles, pedestrians, waves, rain, and winds. These mechanical energy sources can be harvested and reused through appropriate piezoelectric energy conversion to generate considerable electrical energy. As a result, this self-powered mode based on the widespread natural energy could effectively promote the development of sustainable and smart infrastructure.

When subjected to mechanical stress or strain, piezoelectric materials generate charges that can be harnessed and stored using an energy harvesting circuit. For piezoelectric ceramic materials, lead zirconate titanate (PZT) has been widely used to harvest energy under compression or axial applied stress by utilizing its high axial piezoelectric coefficient. Embedded PZT piezoceramic disks into pavements as piezoelectric energy harvesters (PEHs) have been used for road infrastructure energy collection, by which mechanical energy from pavement deformation under moving vehicles can be converted to electrical energy [7–10]. However, the intrinsic brittleness of piezoelectric ceramics has been a consistent issue with PZT, limiting its application on curved surfaces and high strain conditions for energy harvesting. On the contrary, Polyvinylidene Difluoride (PVDF) has the advantage of large compliance, high flexibility, excellent piezoelectric performance, and good fatigue resistance and durability [11], which makes it the most popular commercial flexible piezoelectric polymer for energy harvesting. Significant research has been conducted to harvest vibration energy of PVDF transducer through piezoelectric cantilever beam

* Corresponding author.
E-mail addresses: J.Xie-1@tudelft.nl (J. Xie), y.xu-5@tudelft.nl (Y. Xu), Z.Wan-1@tudelft.nl (Z. Wan), A.Ghaderiaram@tudelft.nl (A. Ghaderiaram), Erik.Schlangen@tudelft.nl (E. Schlangen), B.Savija@tudelft.nl (B. Šavija).

https://doi.org/10.1016/j.enbuild.2023.113582
Received 4 May 2023; Received in revised form 14 August 2023; Accepted 21 September 2023
Available online 27 September 2023

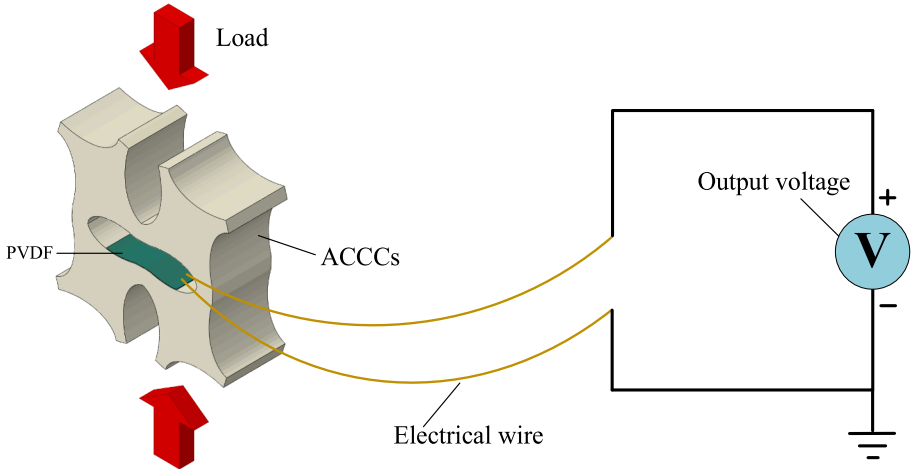

Fig. 1. Schematic of the energy harvesting design of ACCCs.

configurations, including unimorph (a substrate beam with a bonded piezoelectric layer) and bimorph (a substrate beam with two symmetric piezoelectric layers bonded to both sides) devices [12]. A major barrier correlated with vibration-based piezoelectric energy harvesters in civil engineering is that these devices tend to exhibit weak power output since excited frequencies from environmental vibrations are usually away from the resonant frequency of those harvesters. Nevertheless, due to their flexural behaviour, PVDF strain-based energy harvesters have the potential to generate higher voltage. Moreover, thin PVDF films can be flexibly installed in many locations of infrastructures to collect abundant strain energy under a wide range of dynamic loads (e.g., passing vehicles [11], human movements [13–16], rain and wind [17], sound pressure [18]), which can be converted into electrical energy.

Recently, the use of piezoelectric materials for energy harvesting from the mechanical deformation of cementitious materials has gained significant attention due to the widespread availability, exceptional performance, and comparatively low cost of cementitious materials, making them a highly attractive source of energy. Cahill et al. [19] utilized PZT and PVDF to collect mechanical energy from trains passing over a reinforced concrete (RC) bridge at different speeds. The train-induced energy is sufficient to power small wireless sensors used for structural health monitoring (SHM). As for cement-based materials, fiber-reinforced cementitious materials (e.g., strain hardening cementitious composite (SHCC)) are known for tensile strain hardening behavior and excellent crack control capacity [20]. By using fiber-reinforced cementitious materials, a structure can have large deformability and high ductility, which improves the energy harvesting efficiency of using flexible PVDF. Su et al. [21] studied the energy harvesting potential of flexible SHCC incorporating surface-mounted PVDF subjected to four-point bending tests. The maximum cumulative output voltage was reported to reach 17218 mV under a loading rate of 2.0 mm/s. This was attributed to the high strain capacity of SHCC, which allows significant straining (and consequent charging) of the surface mounted PVDF film. Therefore, cementitious composites with high deformation capacity could potentially allow highly efficient energy harvesting with surface mounted PVDF.

Recently it has been shown that fiber-reinforced cementitious materials, such as SHCC, can serve as a ductile matrix for designing materials and structures with unique geometries [22,23] (e.g., metamaterials and metastructures [24]), which offer enhanced deformation and energy dissipation capabilities. This is achieved by making use of additive manufacturing (AM). Additive manufacturing allows for engineering and fabrication of cement-based materials into sophisticated solid and cellular structures with extraordinary properties, known as Architected Cement-based Materials (ACMs). Using additive manufacturing, ACMs with enhanced mechanical properties can be fabricated by tailoring their internal shape, size, and geometry. Moini et al. [25] used 3D printing of hardened cement paste (hcp) elements to design bioinspired Bouligand architectures with high ductility and enhanced work of failure. Sajadi et al. [26] employed cementitious materials to design schwarzite structures that exhibit exceptional resilience and deformation characteristics, thereby improving the ductility, toughness, and energy absorption capacity of cement-based structures.

In our previous study on ACMs, a fiber-reinforced cementitious composite was used as base material to architect mesoscale cellular structures with auxetic behavior, called auxetic cementitious cellular composites (ACCCs). Auxetics are materials that have a negative Poisson's ratio [27]. Auxetic materials exhibit extraordinary mechanical properties, such as high shear resistance [28,29], high indentation resistance [30–32], high energy absorption [12,28,33–35], and high damping capability [36]. Auxetic behavior of the concrete is enabled by controlling the internal cellular structure at millimeter scale, which can be tunably programmed by 3D printing technique [22,37]. When subjected to cyclic loading, the architected ACCCs shows compliant behavior, and a quasi-elastic response which is highly resistant to fatigue. This flexible behavior of ACCCs presents a large deformation with much strain energy, which can be converted into electrical energy via surface-mounted piezoelectric films.

Herein, a novel piezoelectric energy harvester (PEH) design consisting of ACCCs and surface-mounted PVDF was proposed to convert strain-based energy to useable electrical energy, as illustrated in Fig. 1. The ACCCs-PVDF energy harvesting system was first compressed to a certain displacement, and then was subjected to cyclic loading to consistently generate voltage for energy harvesting. A theoretical energy harvesting model regarding this novel design has been established by considering the mechanical–electric coupling in piezoelectric material. The model was validated using experimental data under different loading amplitudes and frequencies.

By integrating fiber-reinforced cementitious materials with auxetic structures via additive manufacturing techniques, ACCCs exhibit a unique second-elasticity behavior characterized by significant deformation capacity. This study introduces an innovative energy harvesting strategy through the incorporation of PVDF films into ACCCs. The energy harvester harnesses the distinctive second-elasticity behavior of ACCCs, offering a new way to convert mechanical energy from significant deformations into practical electrical power. Presumably, the proposed ACCCs-PVDF energy harvesting system can be deployed in coastal areas to harvest kinetic energy from ocean waves. Furthermore, it can be utilized to develop a new generation of shock-absorbing engineered materials arresting systems (EMAS) [38], mitigating the consequences of aircraft landing overruns. This system can also be efficiently employed to absorb impact energy in shock-absorbent bike lane pavements [39].

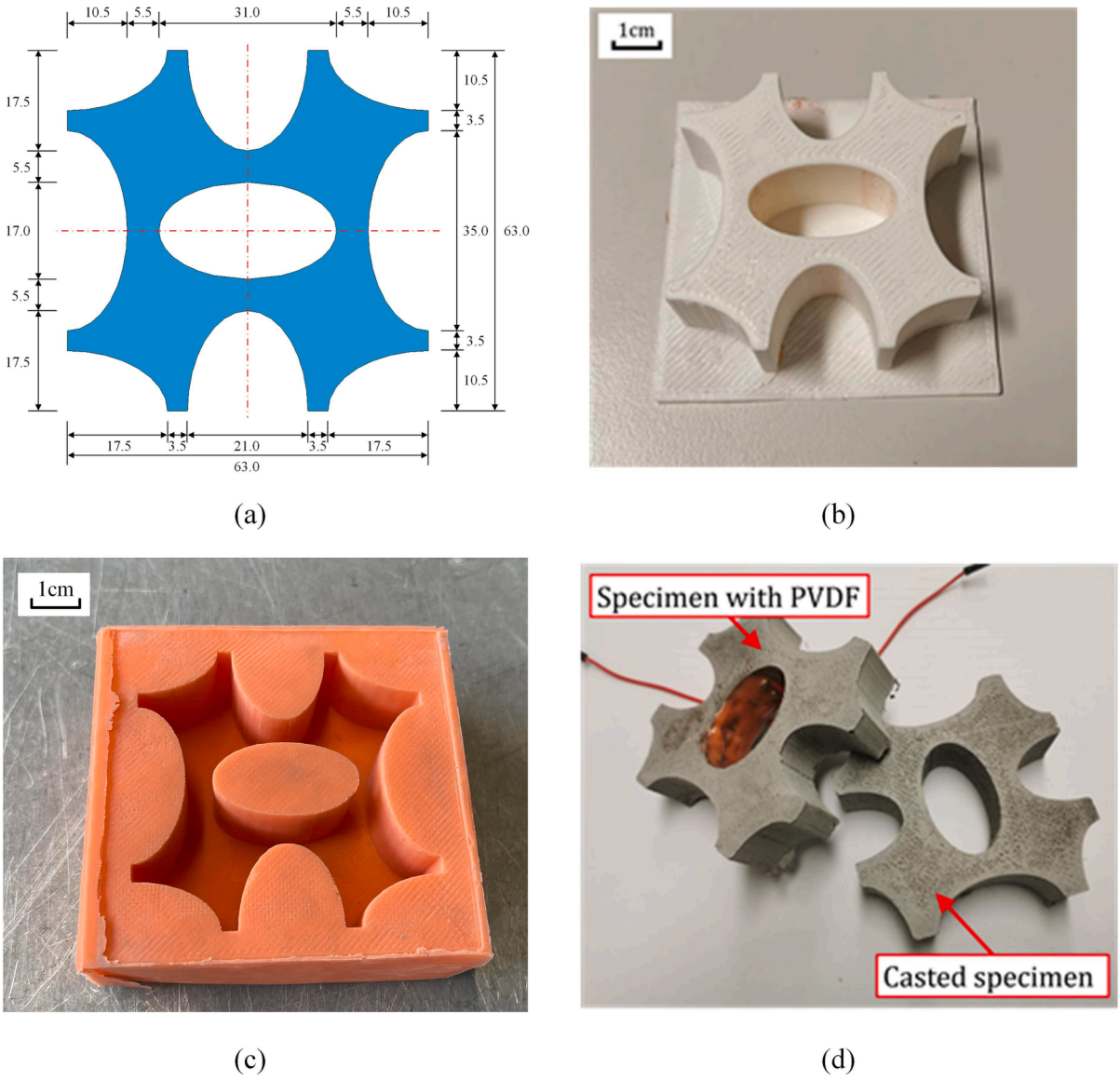

Fig. 2. Schematics of (a) designed dimension, (b) 3D printed ABS unit cell, (c) silicone rubber mold, (d) casted specimen and specimen glued with PVDF film.

Table 1
Mixture proportions of ACCCs (kg/m^3) adopted from [40].

CEM I 42.5 N	Fly ash	Sand (0.125 to 0.250 mm)	Water	Superplasticizer (Glenium 51)	VA	PVA Fiber
471	556	385	428	0.86	0.3	25.6

Note: VA is viscosity modifying agent used for optimizing PVA fiber distribution.

Table 2
Material properties of PVA fibers used in the cementitious matrix (kg/m^3).

Diameter (μm)	Length (mm)	Tensile strength (GPa)	Young's modulus (GPa)	Density (g/cm^3)
15	6	1.6	34	1.28

The renewable energy harvested from these applications can be used to power electronics in infrastructure, contributing to the development of various sustainable and smart infrastructure systems.

2. Experiments

2.1. Sample preparation

A unit cell of the ACCCs was chosen for energy harvesting experiments. The design parameters of the unit cell are shown in Fig. 2. The specimens were created following the so-called "indirect printing" process reported in [22,40]. The procedures are described as follows:

- First, the designed unit cell (shown in Fig. 2a) was 3D printed with a FDM (fused deposition modeling) 3D printer Ultimaker 2+, and ABS (acrylonitrile butadiene styrene) was used as printing material.
- Then printed unit cell (shown in Fig. 2b) is glued in a card box. Subsequently, a two-component silicone rubber (Poly-Sil PS 8510) is mixed (1:1 by mass) and poured in the box.
- After storing in room temperature for two hours, the silicone rubbers solidified. Then the hardened silicone rubber was detached from the box such that a silicone mold was obtained (Fig. 2c).
- Cementitious mixture was casted in the silicone rubber mold. The mixture proportion (listed in Table 1) and mixing procedure of was the same as in our previous work [40]. The properties of PVA fiber

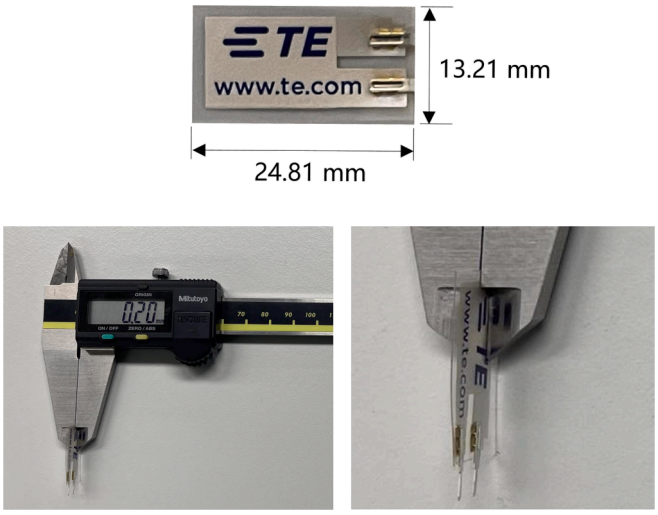

Fig. 3. Geometric measurement for LDT0-028 K PVDF film.

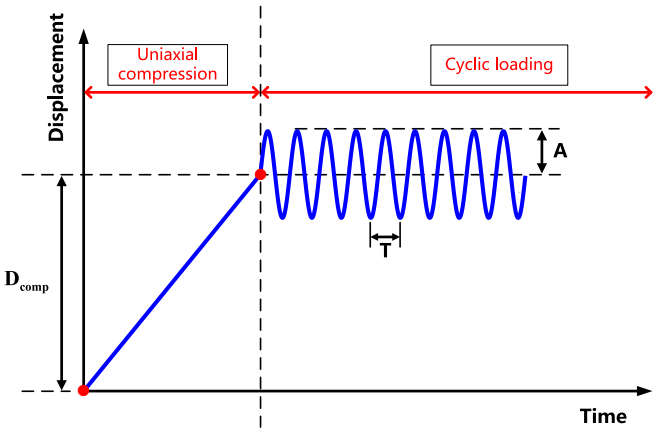

Fig. 4. Loading scheme for energy harvesting experiments.

used in this work were shown Table 2. After curing under room temperature for two days, the specimen (shown in Fig. 2d) was demolded from the silicone mold and stored in the curing chamber (20℃, 96 %RH) until the age of 28 days.

- Two hours before testing, the specimens were taken out of the curing chamber. One PVDF film was wrapped with fabric tape glued by silicone rubber (same as the Poly-Sil PS8510) on the central elliptical hole of each specimen (Fig. 2d) and left for hardening for two hours. As shown in Fig. 3, the LDT0-028 K PVDF film has an area of 24.81 mm × 13.21 mm ($l_p \times w_p$) with a thickness of 0.2 mm (h_p) (including the protective layer against surface oxidation of the silver ink electrode area [21,41,42]). Herein, the piezoelectric layer in the PVDF film has a thickness of 28 μm (t_p).

2.2. Mechanical-electrical tests

The specimens were tested by a hydraulic press INSTRON 8872, with compressive cyclic loadings. Fig. 4 gives the loading scheme for the compressive cyclic tests, which includes two parts of preloading and cyclic loading. During the preloading phase, the unit cell specimen will be first compressed by a displacement loading from zero to D_{com} (5.0 mm); then, based on displacement control, cyclic loading with a constant loading amplitude A will be applied to the unit cell specimen with a frequency f or a period of T by a sinusoidal wave. To investigate the effects of loading amplitude and loading frequency, the amplitudes of 1.0 mm and 2.0 mm, the frequencies of 0.3 Hz, 1.0 Hz and 2.0 Hz were considered in energy harvesting experiments. The open voltage outputted during the cyclic loading test can be used to characterize the energy harvesting capacity of the ACCCs-PVDF system. During the compressive cyclic tests, the digital multimeter was used to simultaneously record the output voltage from the PVDF film. Fig. 5 shows the experimental setup for recording the voltage generated by the ACCCs-PVDF system.

2.3. Experimental results

Fig. 6 shows energy harvesting experiment results of the ACCCs-PVDF system regarding different loading frequencies and loading amplitudes, over a duration of 10 s. In each loading cycle, the output voltage increases as the displacement increases. When reaching the maximum displacement, the ACCC specimen experiences its maximum strain, resulting in the corresponding peak point of the generated output voltage. The output voltage is directly proportional to the applied displacement. Then, when the loading plate slowly moves away from the ACCCs, its strain gradually decreases toward an almost negligible level, mirroring the gradual decrease in the output voltage to nearly zero. Fig. 6 also shows the effects of loading frequency and loading amplitude on the output voltage of the ACCCs-PVDF system. The output voltage decreases with the increase of loading frequency under the same loading amplitude. Further, the voltage increases when the loading amplitude increases from 1.0 mm to 2.0 mm. Comparatively, the effects of loading amplitude on the output voltage are greater than those of loading frequency. At the loading amplitude of 1.0 mm, the maximum output voltages under loading frequencies of 0.3 Hz, 1.0 Hz, and 2.0 Hz were found to be 2.6 V, 2.4 V, and 1.8 V, respectively. Similarly, at the loading amplitude of 2.0 mm, the maximum output voltages under the same loading frequencies were 6.4 V, 5.7 V, and 4.2 V, respectively.

In Fig. 6c, a smooth sinusoidal curve emerges with a loading amplitude of 1.0 mm and a frequency of 0.3 Hz. In contrast, Fig. 6f reveals a nearly sinusoidal voltage pattern under a loading amplitude of 2.0 mm and a frequency of 0.3 Hz, yet it exhibits fluctuations in its peaks. This phenomenon can be attributed to the dynamic interaction

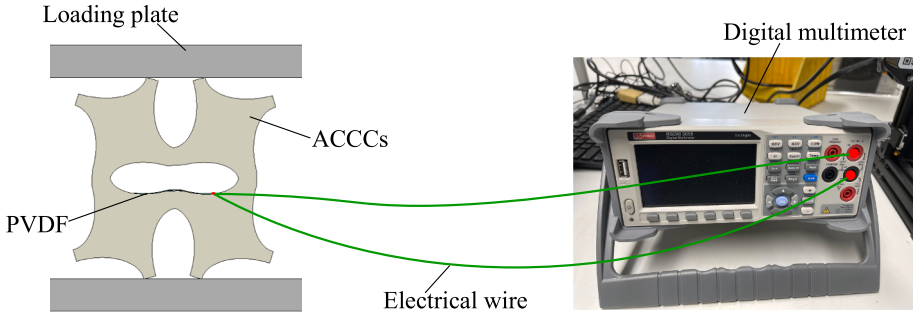

Fig. 5. Schematic of the energy harvesting test for the ACCCs-PVDF system.

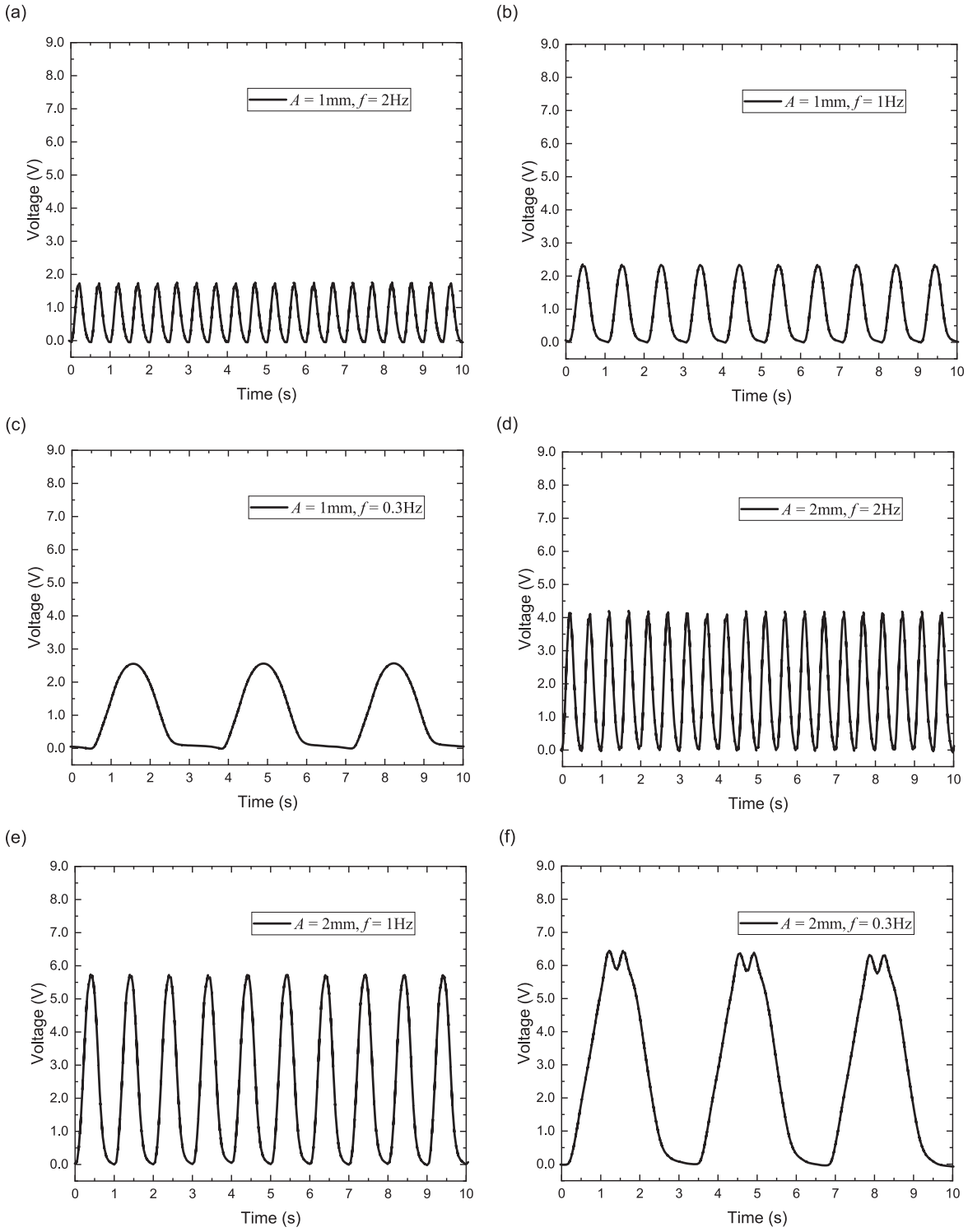

Fig. 6. Energy harvesting experiment results of the ACCCs-PVDF system regarding different loading frequencies and loading amplitudes.

between ACCCs and the PVDF film, leading to localized sliding effects and subsequent peak fluctuations. Therefore, the generated voltage experiences variations in its peak values. This sliding-induced effect on the observed output voltage becomes more pronounced with higher loading amplitudes.

3. Numerical modeling

3.1. Overview

Fig. 7 gives a flowchart of the energy harvesting model for the ACCCs-PVDF system. The mechanical model of ACCCs consists of two parts, preloading and cyclic loading. During the preloading phase, concrete damage plasticity (CDP) model was used to quantify the mechanical behavior of ACCCs. Due to its limitations, the CDP model was

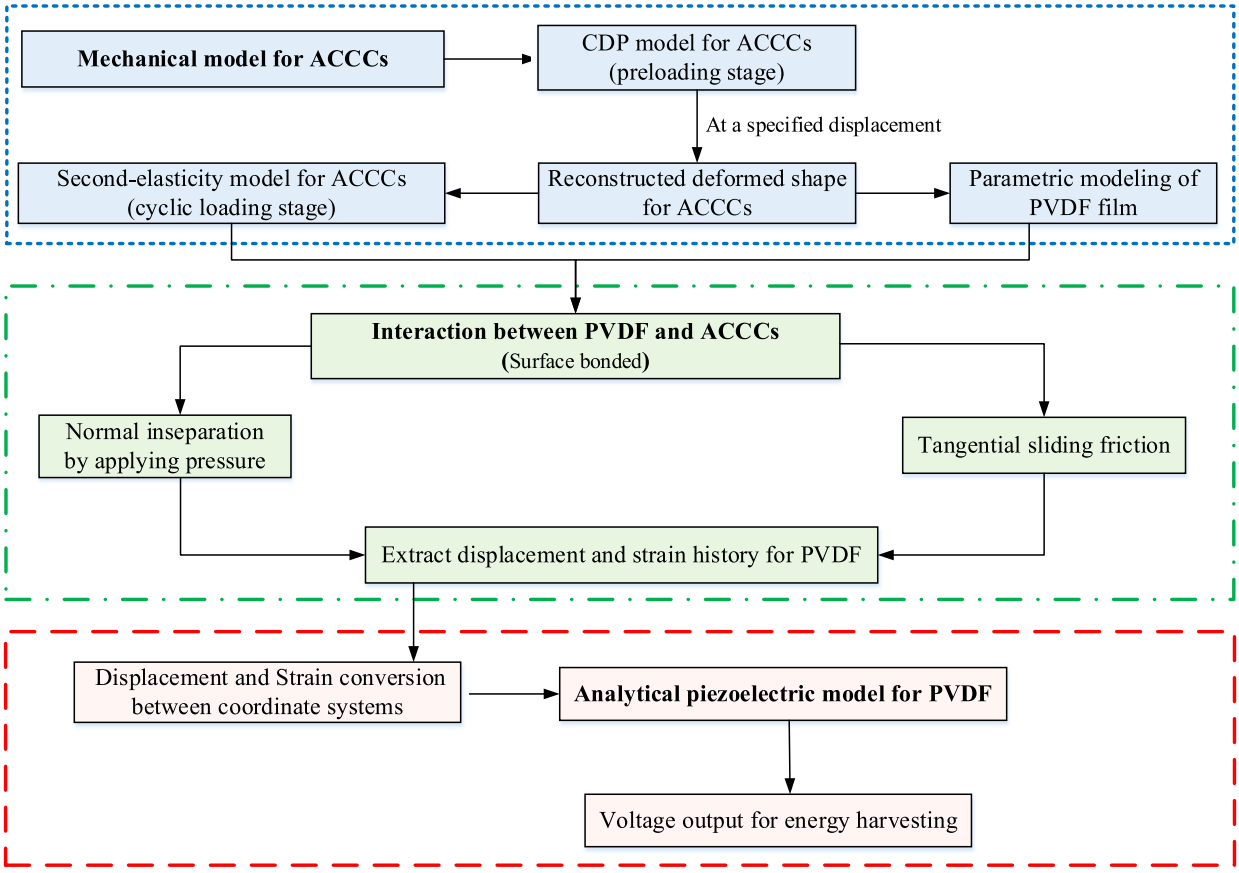

Fig. 7. Flowchart of the energy harvesting model for ACCCs-PVDF system. The blue box consists of the steps for the mechanical modeling. The green box consists of the steps to consider the interaction between PVDF and ACCCs. The red box consists of the steps to conduct the piezoelectric modeling. (For interpretation of the references to colour in this figure legend, the reader is referred to the web version of this article.)

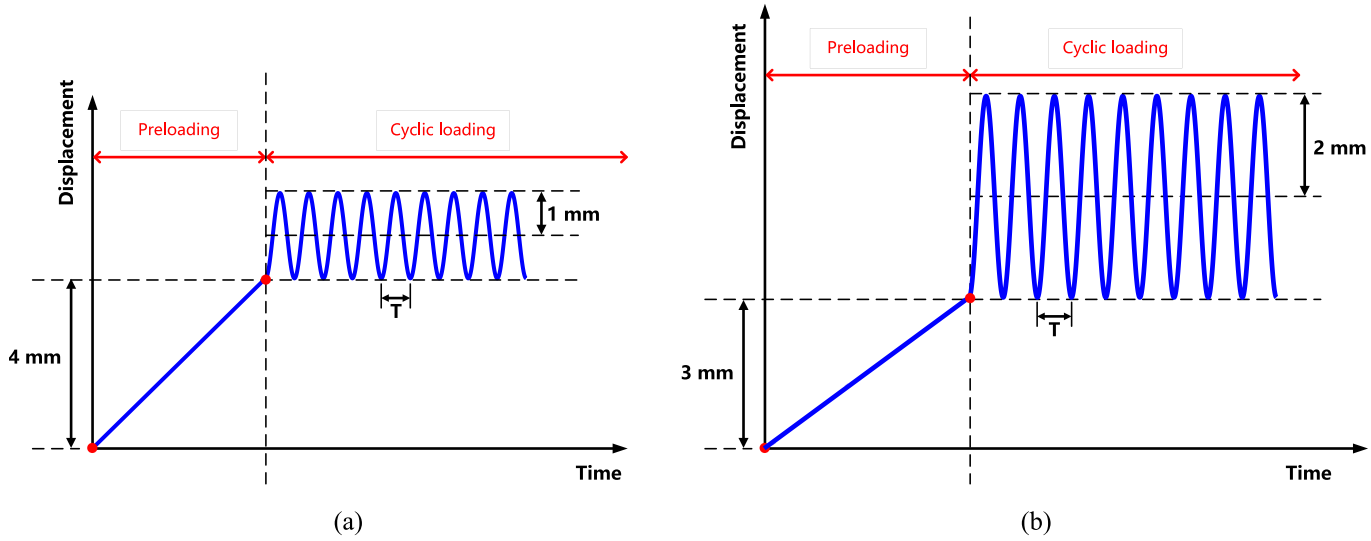

Fig. 8. Loading plans for energy harvesting models, (a) amplitude 1.0 mm, (b) amplitude 2.0 mm.

unable to simulate the second-elasticity behavior of the ACCCs during cyclic loading (see **Appendix A**). Instead, the second-elasticity model was used to characterize the elastic behavior. To enable the conversion between the CDP and second-elasticity models, the deformed shape of the ACCCs at a specific loading displacement calculated by the CDP model was reconstructed as the initial geometry for the second-elasticity model. Afterwards, the interaction between PVDF and ACCCs was considered for the strain transfer, as shown in the green box of Fig. 7. Then, the mechanical response of the PVDF film was extracted to calculate the output voltage, based on the analytical piezoelectric model of PVDF film (the red box of the Fig. 7).

Compared with the experimental loading plan in Fig. 4, corresponding loading plans for energy harvesting with different amplitudes have been adopted in models, as shown in Fig. 8. In the energy

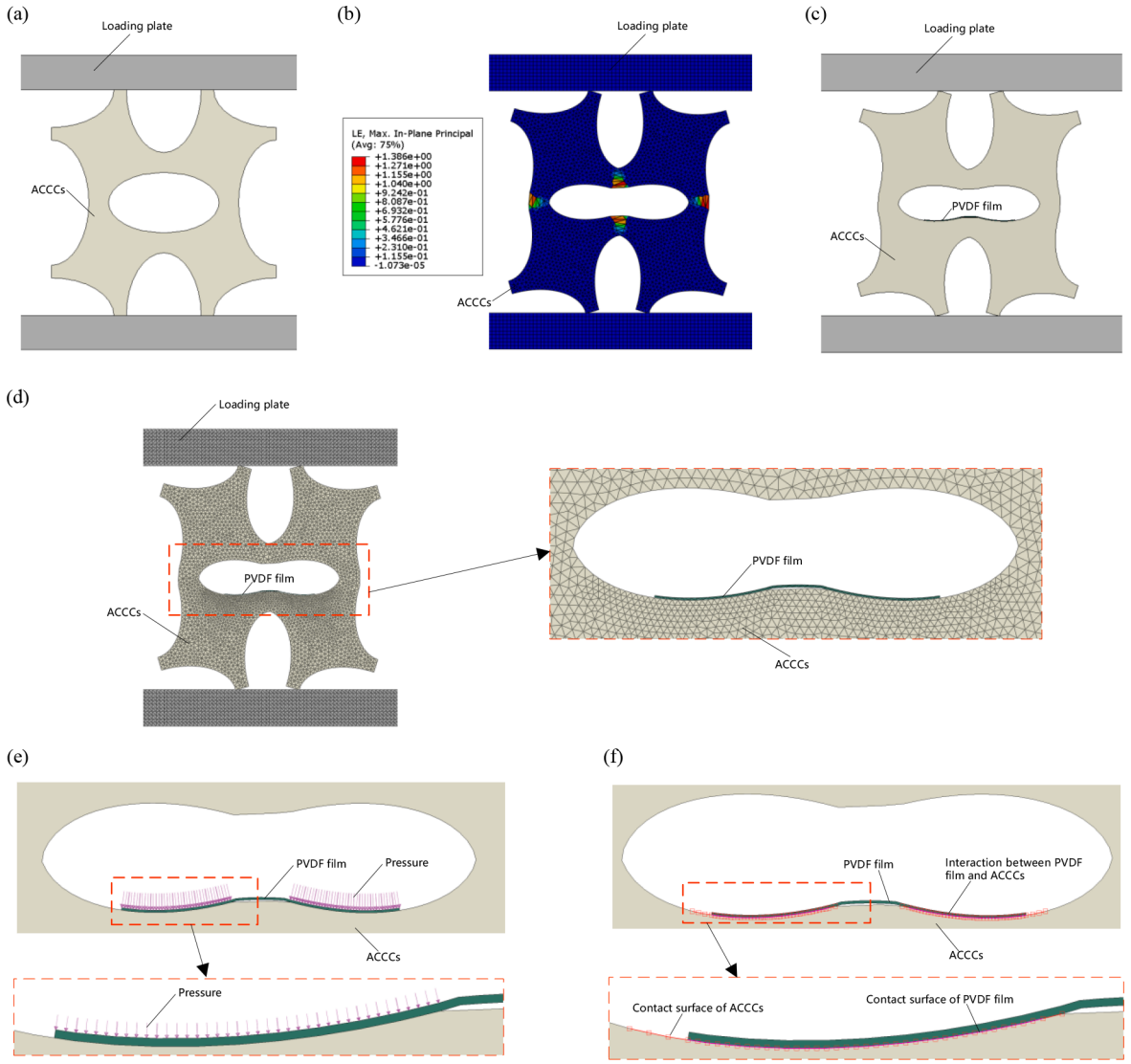

Fig. 9. Modelling of energy harvesting with ACCCs and surface-mounted PVDF, (a) initial shape before preloading, (b) deformed shape at the displacement of 4.0 mm, (c) reconstructed shape for cyclic loading, (d) finite meshing and PVDF film configuration for cyclic loading, (e) normal pressure applied on PVDF film for simulating normal inseparability, (f) interaction between PVDF film and ACCCs.

Table 3
CDP model parameters for ACCCs.

ρ(kg/m^3)	E_0(MPa)	ν	σ_{b0}/σ_{c0}	K_c	ψ	ε_{ec}	Viscosity Parameter
1870	8230	0.2	1.16	0.667	35	0.1	0.001

Table 4
Tensile behavior parameters for ACCCs.

Yield Stress (MPa)	Cracking Strain (%)
1.74	0
0.50	0.05
1.08	0.26
1.08	0.48
0.85	0.73
0.49	1.17
0.10	2.00

Table 5
Compressive behavior parameters for ACCCs.

Yield Stress (MPa)	Inelastic Strain (%)
12.16	0
20.53	1.49
15.06	6.39
14.08	13.13
14.46	18.21
14.47	24.56

harvesting experiments, the specimens were first pre-compressed during the uniaxial compression test until the displacement reaches 5.0 mm. For convenience, the deformed geometry of the specimen at the displacement of 4.0 mm was reconstructed as the initial shape for cyclic loading, since the range from the displacement of 4.0 mm to 5.0 mm belongs to the second-elasticity range. Furthermore, during the cyclic loading test with a 1.0 mm amplitude, the specimen becomes stress-free at a displacement of 4.0 mm because of the loading plate detaching from the specimen. Correspondingly, the reconstructed model has no initial stress before cyclic loading. Similarly, for the cyclic loading test with an

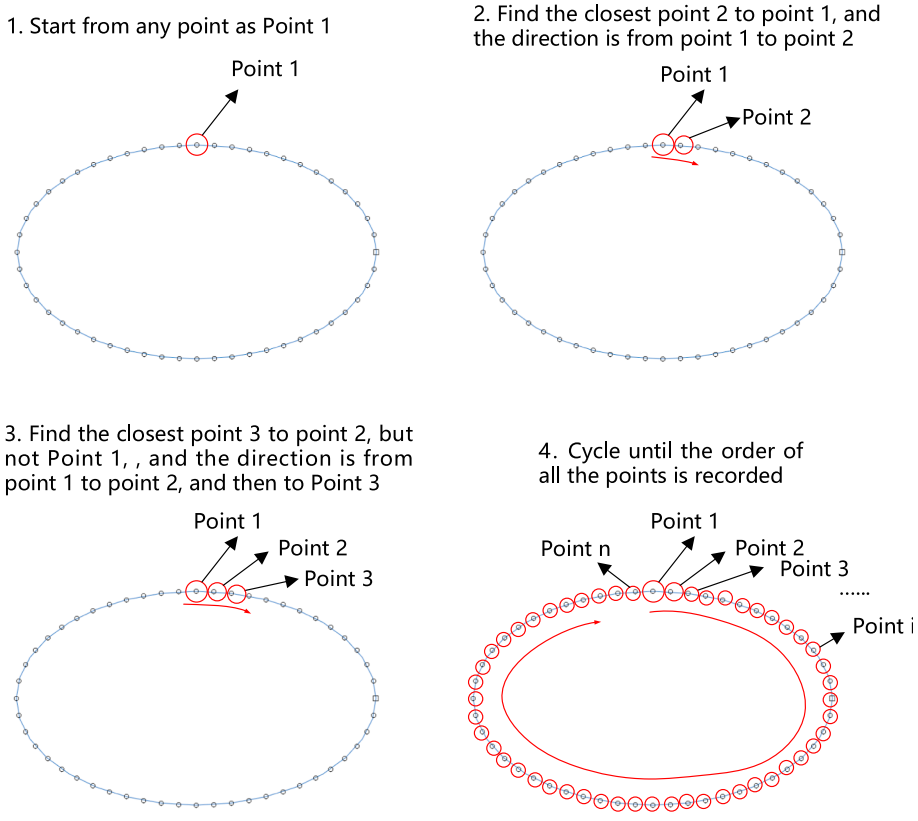

Fig. 10. Topological reconstruction of geometric shapes based on node-order-track algorithm.

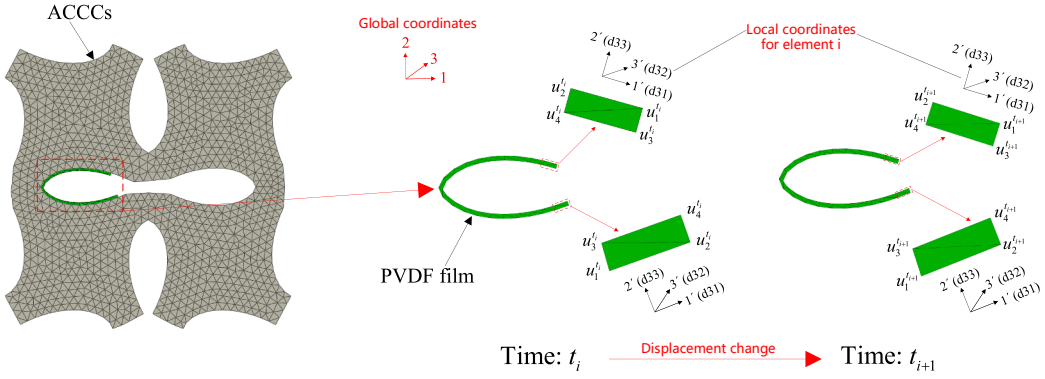

Fig. 11. Subdivided piezoelectric film for analytical calculation.

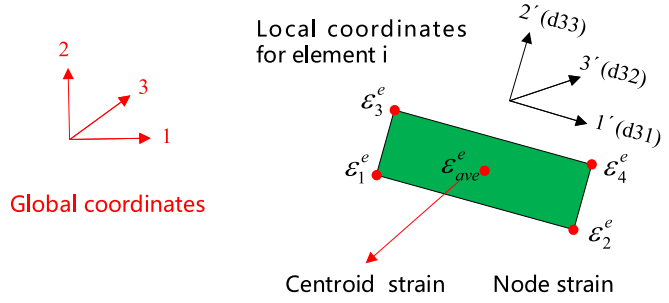

Fig. 12. The centroid strain of each rectangular block by an averaging method.

Table 6
Piezoelectric properties and mechanical properties of PVDF.

Material properties	Value	Units	Material properties	Value	Units
ρ_p	1780	kg/m^3	E_p	2	GPa
ν_p	0.34	–	f_{eu}	45–55	Mpa
d_{31}	23	pC/N	d_{32}	1.476	pC/N
d_{33}	–33.8	pC/N	d_{15}	20	pC/N
e_{33}	1.15e^{-10}	F/m	k_{31}	12%	–

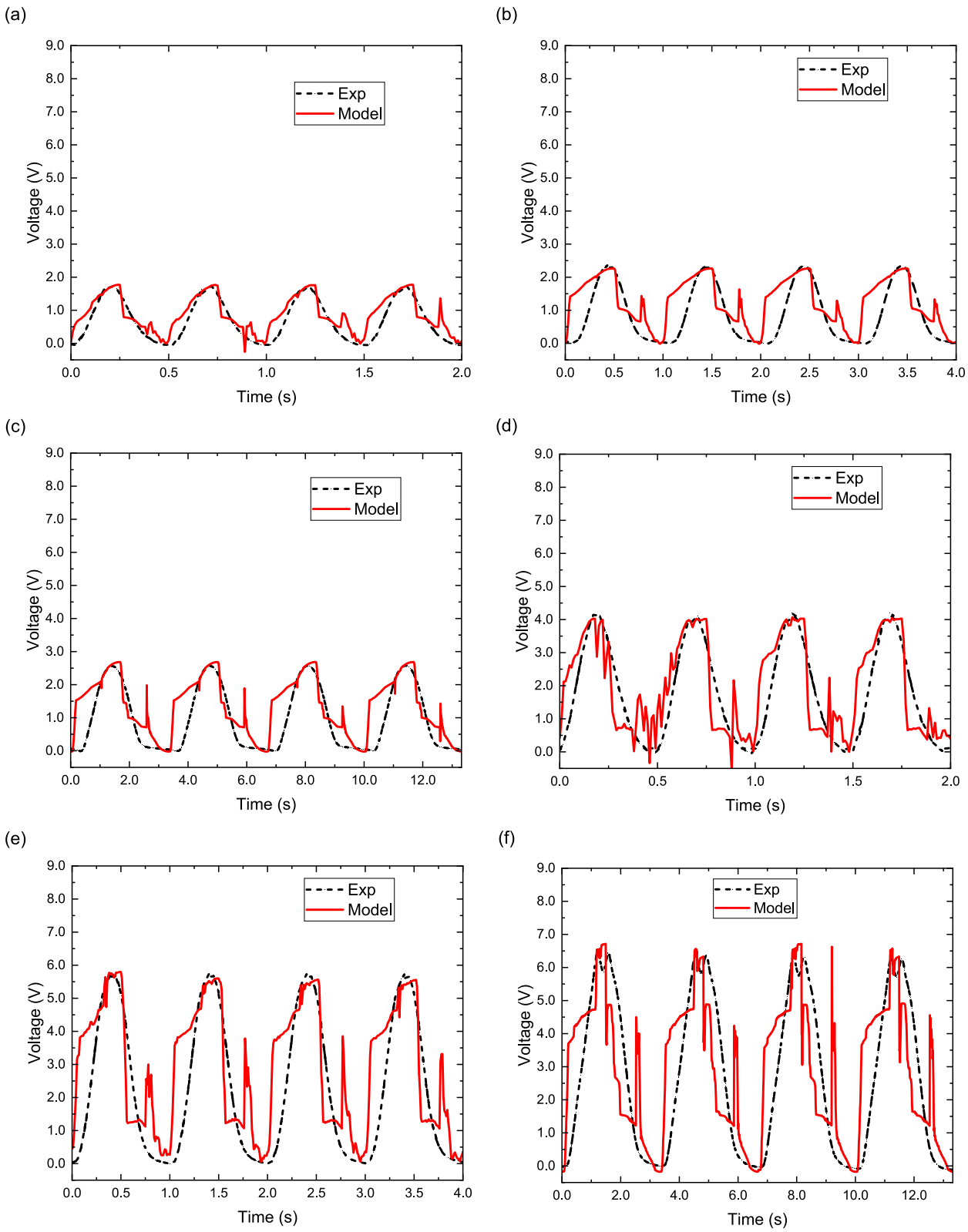

Fig. 13. Comparisons of the output voltage between simulated results and experimental data under different loading frequencies and different loading amplitudes, (a) A = 1.0 mm, f = 2 Hz, (b) A = 1.0 mm, f = 1 Hz, (c) A = 1.0 mm, f = 0.3 Hz, (d) A = 2.0 mm, f = 2 Hz, (e) A = 2.0 mm, f = 1 Hz, (f) A = 2.0 mm, f = 0.3 Hz.

amplitude of 2.0 mm, the deformed geometry of the specimen at the displacement of 3.0 mm was chosen as the initial shape for cyclic loading. While the first cycle is somewhat influenced by the boundary conditions, the stable voltage magnitudes of energy harvesting results from the second cycle onwards were extracted for analysis with zero volt as a benchmark.

Table 7
Friction coefficients under different loading amplitudes and loading frequencies.

Loading amplitude	1.0 mm			2.0 mm		
Loading frequency	0.3 Hz	1.0 Hz	2.0 Hz	0.3 Hz	1.0 Hz	2.0 Hz
Friction coefficients	0.146	0.135	0.080	0.500	0.452	0.300

3.2. Mechanical model

3.2.1. CDP model for preloading

The elastic–plastic behavior of cementitious composites reinforced by PVA (Polyvinyl alcohol) fibers can be simulated by CDP model. The theory of using CDP model for simulating the mechanical behavior of ACCCs has been presented in our previous work [37]. As seen in Fig. 9a, b, during the preloading stage, the mechanical behavior of ACCCs is modeled based on CDP model from zero to a certain loading displacement. The deformed specimen with strain (LE) distribution at the displacement of 4.0 mm was displayed in Fig. 9b when the loading amplitude is 1.0 mm.

The CDP model parameters for the ACCCs were listed in Table 3. There, ρ refers to the density of the ACCCs. E_0 is the initial elastic modulus of the ACCCs. ν is the Poisson's ratio of the ACCCs. σ_{b0}/σ_{c0} is the ratio between the initial yield stress in equi-biaxial compression and uniaxial compression. K_c represents the ratio of the second stress invariants on the tensile and compressive meridians. ψ refers to the dilation angle. ε_{ec} is the flow potential eccentricity. For the material parameters of CDP model, tensile behavior parameters and compressive behavior parameters for the ACCCs were listed in Table 4, Table 5, respectively. The CDP model parameters for the ACCCs under tension and compression have been calibrated by using experimental results of uniaxial tension and compression tests in our previous study [22,37]. The loading plate is made of steel with the elastic modulus of 198.0 GPa, the Poisson's ratio of 0.3 and the density of 7900 kg/m^3.

The CDP model of ACCCs under quasi-compression was simulated using the ABAQUS/explicit module. The meshing of the ACCCs specimen was achieved using CPS3, a 3-node linear plane stress triangular element without hourglass effect. An analysis of mesh size dependence was conducted to ascertain the optimal mesh configuration. A quasi-static displacement was imposed on the top plate in the direction of compression. The bottom plate remained fixed. In our previous compression experiments for ACCCs [37], we employed plastic films to minimize friction between the ACCCs specimen and the loading plates. Consequently, a low friction coefficient of 0.105 was adopted to simulate the slight friction between the specimen and the loading plates. To minimize the overclosure between the specimen and the loading plates, a hard contact approach was implemented.

3.2.2. Reconstruction of ACCCs

As displayed in Fig. 7c, the deformed shape of ACCCs at a certain loading displacement will be reconstructed by topological information as the initial geometry for the cyclic loading. As shown in Fig. 10, a new algorithm called node-order-track algorithm was developed to conduct topological reconstruction of geometric shapes at a specific time of loading process. The algorithm reconstructs the geometric shape based on topological information (i.e., node order recorded) and node coordinates at the current moment. The current node coordinates are obtained by adding the corresponding displacements to the original coordinates. The node-order-track algorithm is used to extract the deformed geometric profile of ACCCs at a certain loading displacement by Python-based programming in ABAQUS. As displayed in Fig. 9c, when the displacement reached 4.0 mm, the deformed shape at this moment was reconstructed as the initial shape for cyclic loading with the loading amplitude of 1.0 mm. Similarly, the deformed shape at the displacement of 3.0 mm was reconstructed as the initial shape for cyclic loading with the loading amplitude of 2.0 mm. The geometric entity enclosed by the extracted profile is then generated and meshed with the same element type but different element distribution or topology information (see Fig. 9d).

3.2.3. Second-elasticity model of ACCCs

During the uniaxial compression test, the second-elasticity phenomenon of ACCCs can be observed from the stress–strain curve in our previous study [22,43], as shown in **Appendix A**. The range of second-elasticity in ACCCs was utilized for energy harvesting via cyclic loading. Here, the ACCCs will be considered as a second-elasticity model with an equivalent structural elastic modulus of the whole unit cell during the cyclic loading stage, as elucidated in Figs. 7, 9c. To this end, the reconstructed geometric shape of ACCCs at a certain loading displacement (i.e., the end of preloading stage) is used as the initial shape for second-elasticity model during cyclic loading. For the material properties, the elastic modulus of the based material of the ACCCs in the second-elasticity model was taken as 1825 MPa, as indicated in **Appendix A**. The Poisson's ratio of the base material is 0.2. During cyclic loading simulation, a sinusoidal displacement consistent with the loading scheme employed in cyclic tests was applied to the top plate, while the bottom plate remained fixed. The interaction between the specimen and the loading plates was maintained as established in the compression model.

3.2.4. Parametric modeling of PVDF film

The energy harvesting is only considered in the second-elasticity phase. Thus, the modeling of the PVDF film for energy harvesting is only considered in the second-elasticity stage, as illustrated in the blue box of Fig. 7. The PVDF film undergoes a small strain with a large displacement due to its flexural behavior. Therefore, the size of the curved PVDF film attached on the central elliptical hole of ACCC specimen remains consistent with its original size. As the PVDF film is an elastic material, its output voltage is governed by the extent of strain variation, which remains independent of its strain history. This strain variation is determined by how the film deviates from its original curvature during deformation. Thus, the initial curvature of the PVDF film will affect the output voltage. The parametric modeling of the PVDF film was based on the reconstructed shape of the ACCCs (**Appendix B**). The internal profile of the deformed ACCCs in Fig. 9c was chosen and translated inward by a thickness of PVDF film (0.2 mm) to obtain the whole PVDF film, which can be tailored according to the length of PVDF film and the bonded position of PVDF film. Then, the flat middle part of the PVDF film was modified to a transition arc by smoothing with the δ_p of 0.025 (the shape parameter defined in **Appendix B**). The PVDF film configuration via parametric construction above can be seen in Fig. 9d. In the mechanical model, the PVDF film is considered isotropic due to small strain.

3.2.5. Interaction between ACCCs and PVDF

In FEM, the general method considering normal inseparability of contact elements mainly constrains their relative normal displacement by penalty function. This is efficient when the contact surface is close to the plane wherein contact elements do not have significant relative movement differences along their normal direction. However, this method is limited when the surface has a greater curvature, which was presented in **Appendix C**. To ensure that the PVDF film maintains normal contact with the ACCCs, a new modeling approach was developed that considers the consistent normal inseparability of contact elements along the curved surface. By applying a certain pressure in the normal direction of contact elements, the PVDF film and ACCCs will not be separated in the normal direction, as illustrated in Fig. 9e. Simultaneously, the PVDF film is able to maintain a certain level of sliding along the curved surface of the ACCCs. The application of pressure to various positions (i.e., contact elements) can also be utilized to consider different de-bonding conditions. Furthermore, within the elastic range of the ACCCs-PVDF system, the applied pressure does not result in a change in the amplitude of strain. Consider the bonding condition

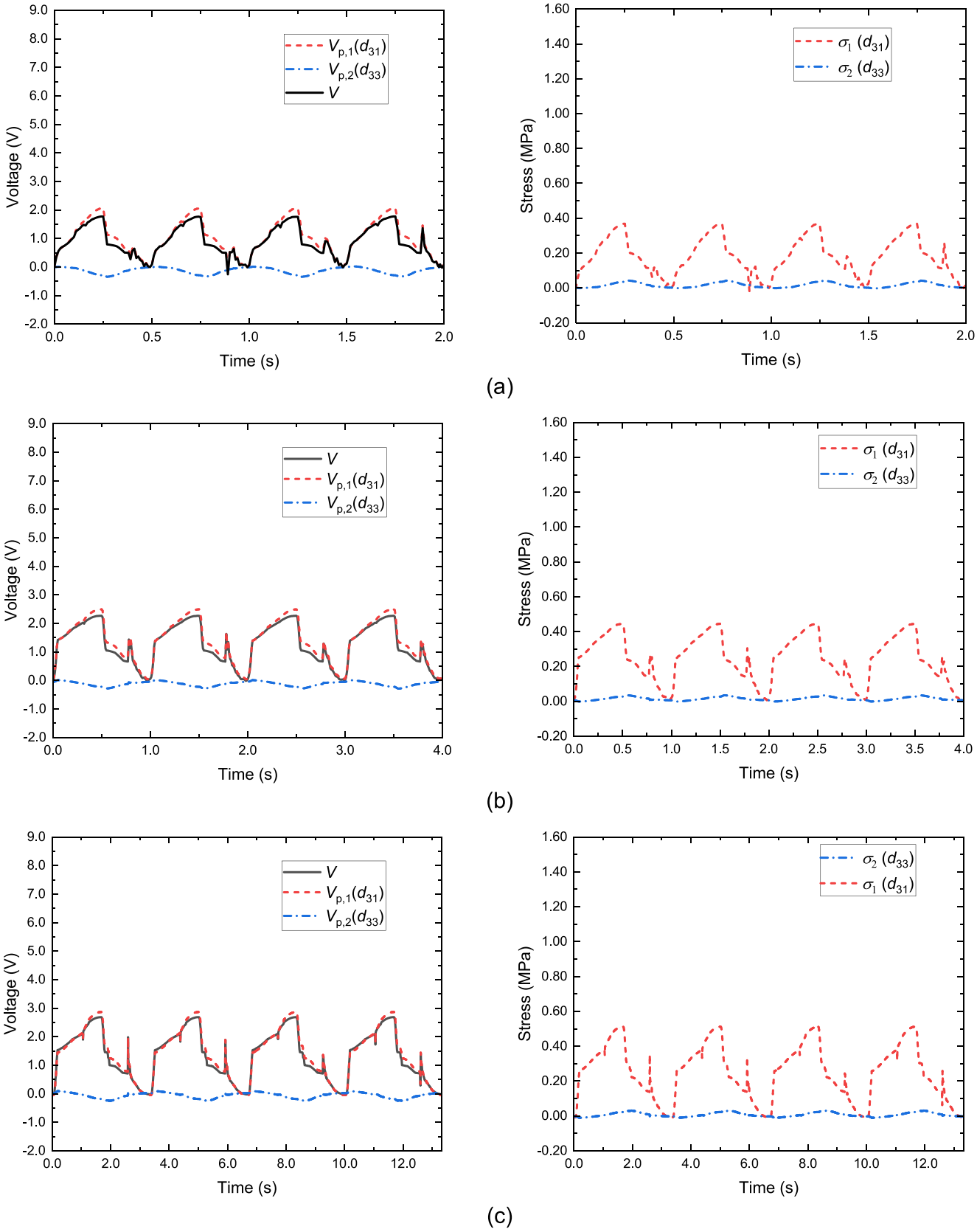

Fig. 14. Voltage components and stress components generated by d_{31} and d_{33} under different frequencies with the loading amplitude of 1.0 mm, (a) A = 1.0 mm, f = 2.0 Hz, (b) A = 1.0 mm, f = 1.0 Hz, (c) A = 1.0 mm, f = 0.3 Hz.

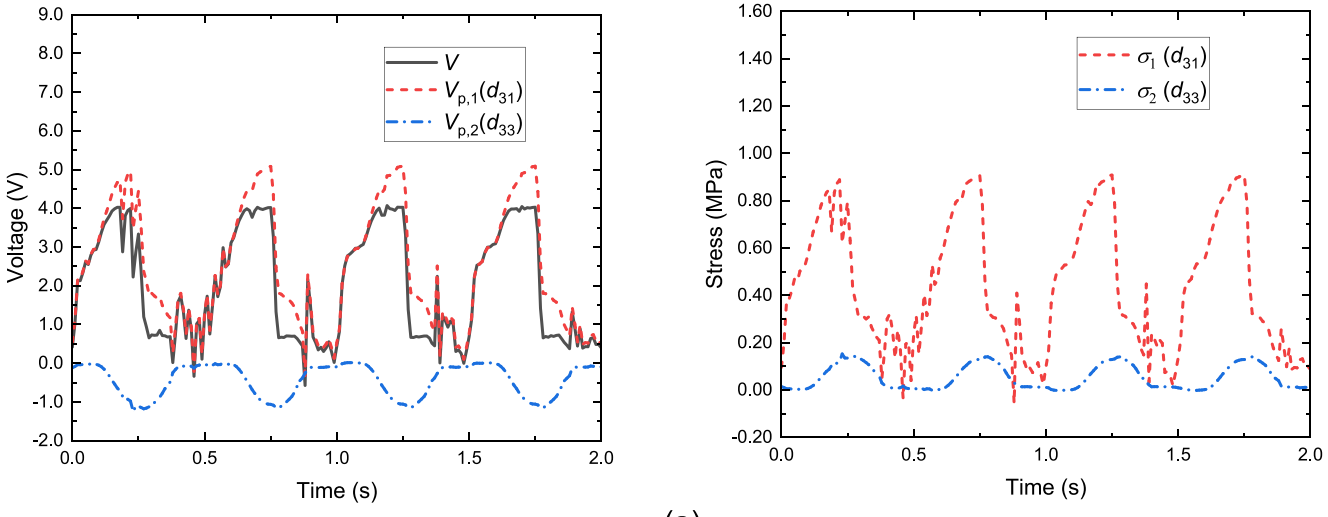

(a)

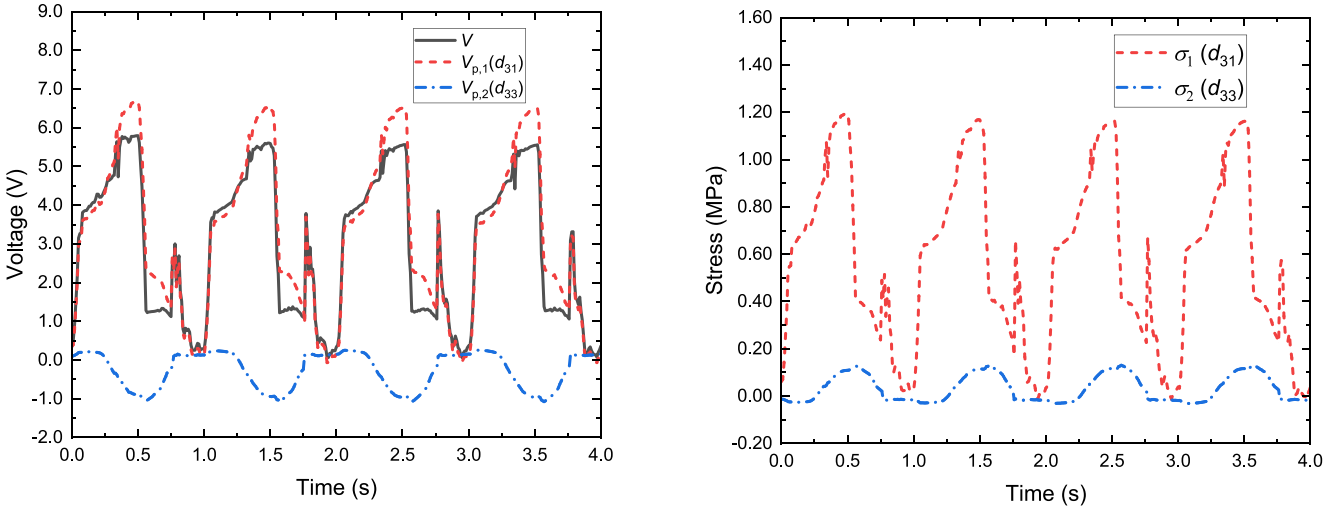

(b)

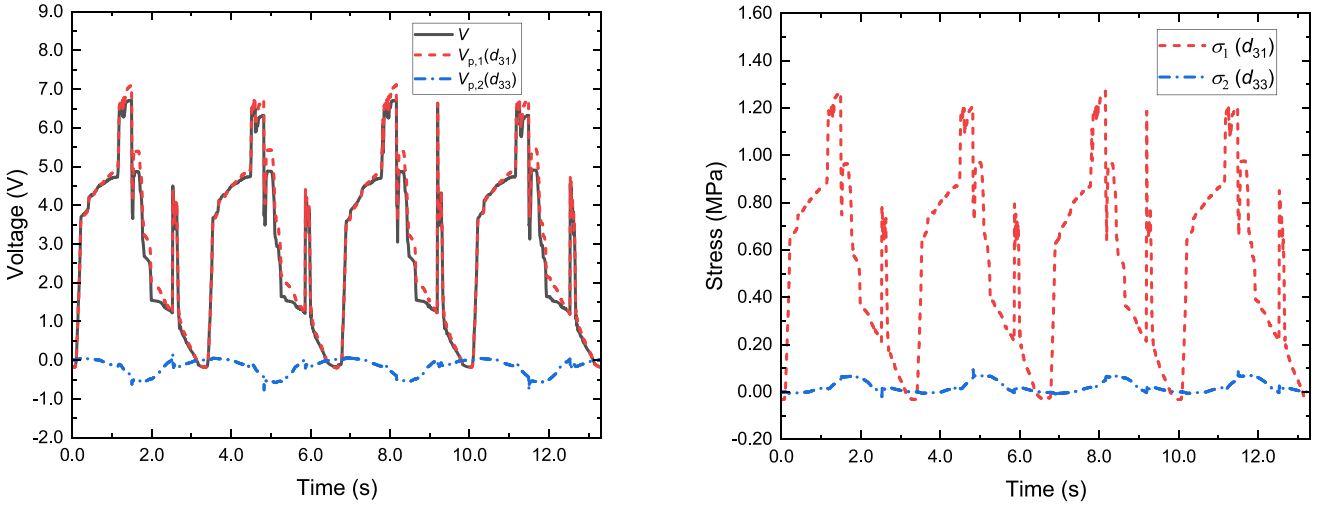

(c)

Fig. 15. Voltage components and stress components generated by d_{31} and d_{33} under different frequencies with the loading amplitude of 2.0 mm, (a) A = 2.0 mm, f = 2.0 Hz, (b) A = 2.0 mm, f = 1.0 Hz, (c) A = 2.0 mm, f = 0.3 Hz.

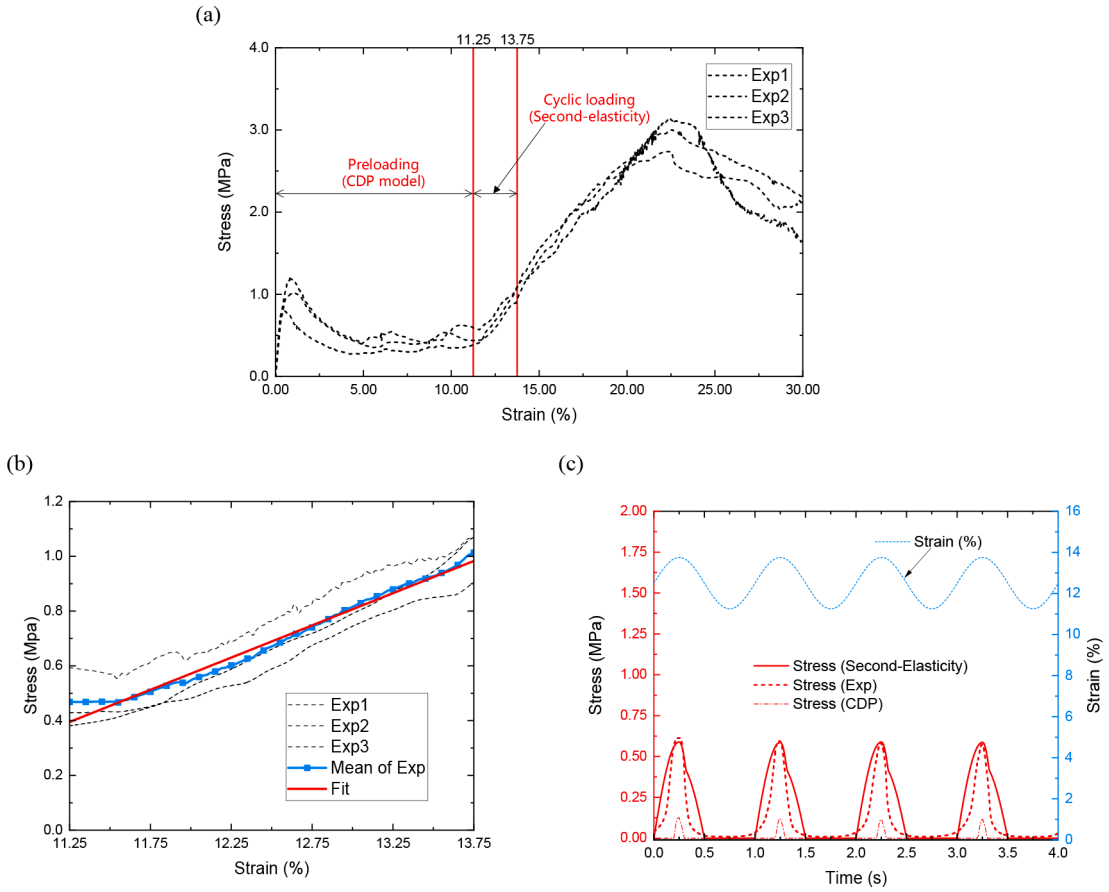

Fig. A1. Material parameter for second-elasticity model of ACCCs, (a) the stress–strain curve of the ACCCs under uniaxial compression test, (b) fit of the elastic modulus for second-elasticity of ACCCs, (b) comparison of CDP model, second-elasticity model, and experiments regarding strain and stress results during cyclic loading.

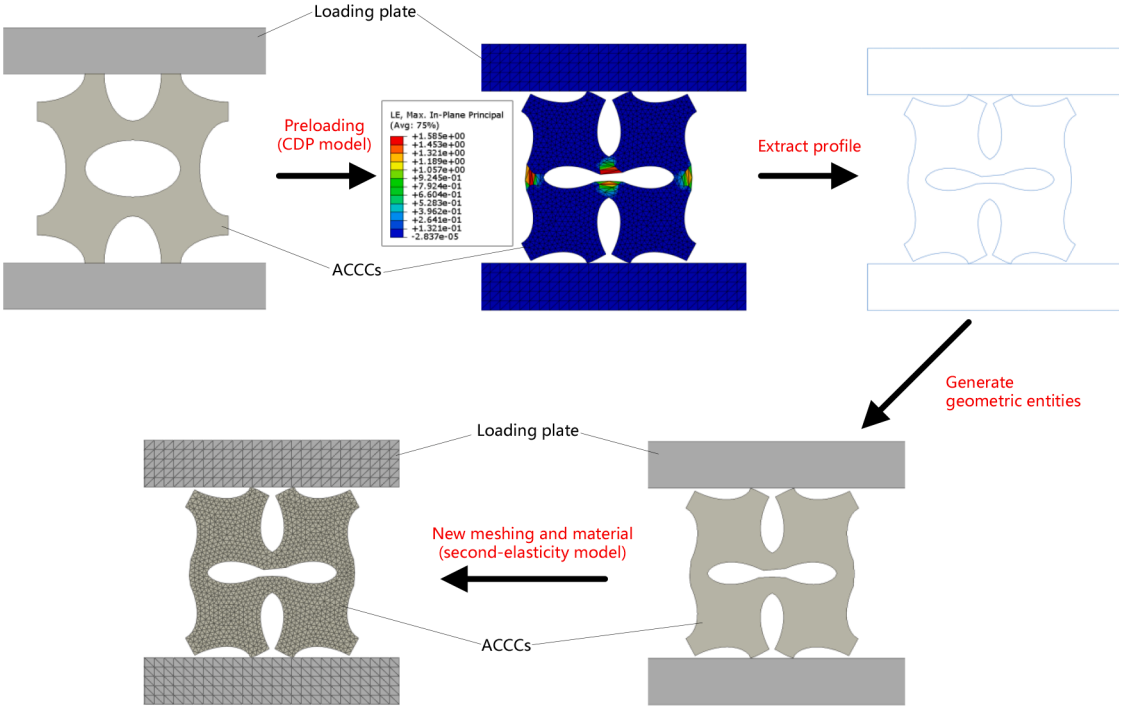

Fig. A2. Topological reconstruction of ACCCs at a certain loading displacement.

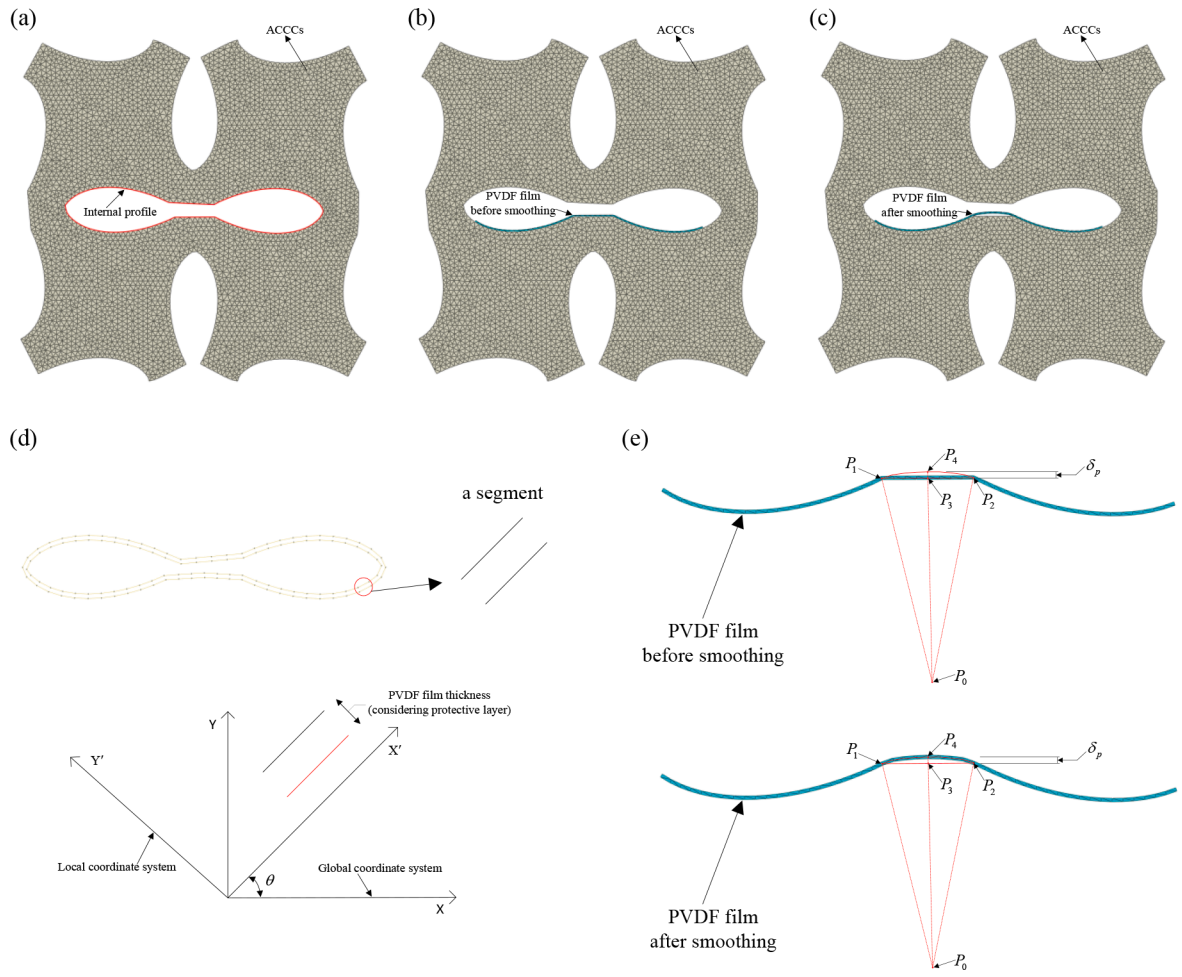

Fig. B1. Parametric modeling for PVDF film, (a) internal profile of the specimen, (b) PVDF film construction before smoothing, (c) PVDF film construction after smoothing, (d) coordinates conversion between different coordinate system, (e) geometry information used for PVDF film smoothing.

during cyclic loading, the pressure of 0.035 MPa was applied to prevent the separation of PVDF film and ACCCs. As seen in Fig. 9e, the transition arc in the middle of the PVDF film was not applied pressure due to the presence of cracks in the middle region of the ACCCs. The tangential sliding friction coefficient in the energy harvesting model was determined by comparison with experiment results regarding the output voltage. Fig. 9f displayed the contact surface of the ACCCs and contact surface of PVDF film for considering their mechanical interaction. The mesh in the region where the interaction occurs is refined to ensure the computational accuracy, as indicated in Fig. 9d. Geometric nonlinearity was not considered since the elastic analysis during cyclic loading has no residual effect on subsequent steps. The interaction between the PVDF film and ACCCs was simulated using the surface-to-surface interaction in ABAQUS. To ensure result accuracy, the ABAQUS/explicit module with double-precision analysis was employed.

3.3. Analytical formulas for piezoelectric model

The mechanical response of the bonded PVDF film can be obtained from the mechanical model of the ACCCs-PVDF system presented above. On this basis, analytical formulas for piezoelectric model have been developed for calculating the output voltage due to piezoelectric effects of the PVDF film, as seen in the red box of Fig. 7. The PVDF film used in the study has a curved shape, which makes it challenging to apply piezoelectric formulas. To overcome this challenge, the film needs to be divided into straight rectangular segments, which allows for easier application of the piezoelectric formulas. This is schematically illustrated in Fig. 11. Herein, each rectangular segment consists of two triangular elements (the element type for meshing) with four nodes. As shown in Fig. 11, four nodes of each rectangular segment have time-dependent displacements as $u_1^{t_i}$, $u_2^{t_i}$, $u_3^{t_i}$, $u_4^{t_i}$ at time t_i and $u_1^{t_{i+1}}$, $u_2^{t_{i+1}}$, $u_3^{t_{i+1}}$, $u_4^{t_{i+1}}$ at time t_{i+1}. In Fig. 11, the piezoelectric strain coefficient d_{31} relates the generated electric charge in the thickness direction to the applied stress along the length direction (piezoelectric mode 31). The piezoelectric strain coefficient d_{33} relates the generated electric charge in the thickness direction to the applied stress along the thickness direction (piezoelectric mode 33). For most rectangular segments, their local coordinate systems are different from the global coordinate system, and change over time. The directions of the local coordinate system of each rectangular segment can be calculated by the displacements of the four nodes for later coordinates conversion. The PVDF film was meshed by triangular elements, and thus each rectangular segment is comprised of two triangular elements. The centroid strain of the rectangular segment is an average value of the four node strains of the two triangular elements, as indicated in Fig. 12. Then, the centroid strain of each rectangular segment in the global coordinate system should be converted to the strain in its local coordinate system, as shown in Fig. 11.

The strain $\varepsilon_m^{'}$ in the local coordinate system can be obtained via the strain ε_m in the global coordinate system. Detailed derivation of formulas can be found in **Appendix D**.

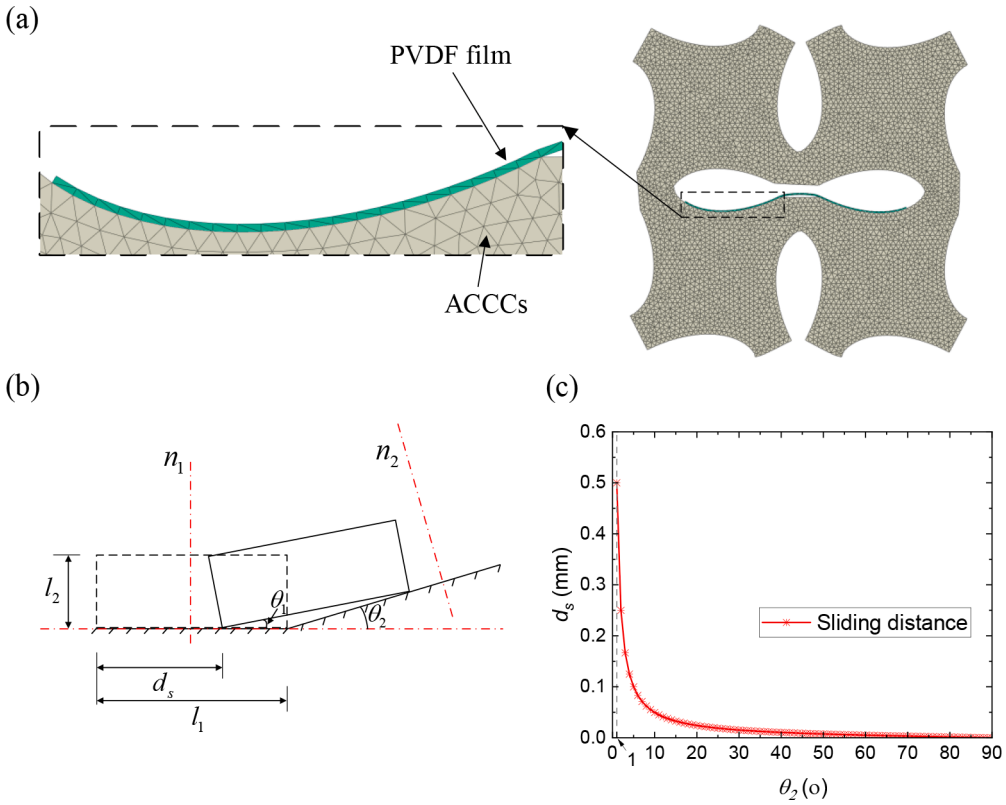

Fig. C1. Limitations for normal inseparability based on displacement penalty method, (a) curved surface between ACCCs and PVDF film, (b) theoretical mechanism of displacement penalty method, (c) the variation of d_s versus θ_2 when PVDF film slides forward at the θ_1 of 1.0°.

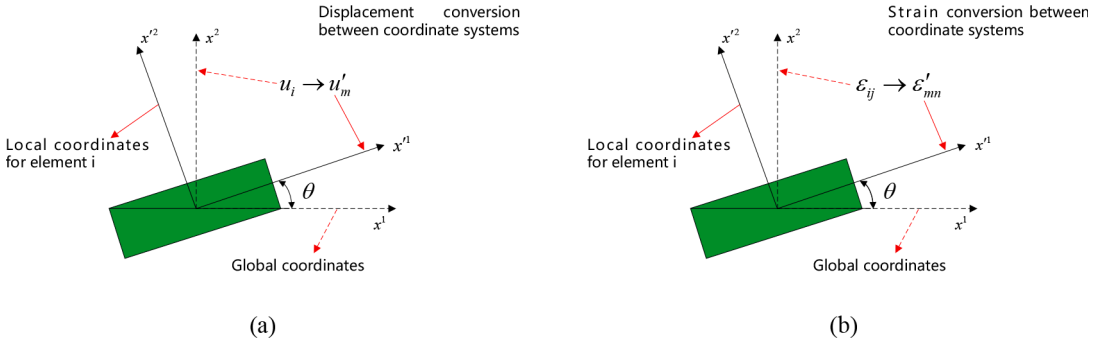

Fig. D1. Component conversion between coordinate systems, (a) displacement, (b) strain.

$$\begin{bmatrix} \varepsilon'_{11} & \varepsilon'_{12} \\ \varepsilon'_{21} & \varepsilon'_{22} \end{bmatrix} = \begin{bmatrix} \cos\theta & \sin\theta \\ -\sin\theta & \cos\theta \end{bmatrix} \begin{bmatrix} \varepsilon_{11} & \varepsilon_{12} \\ \varepsilon_{21} & \varepsilon_{22} \end{bmatrix} \begin{bmatrix} \cos\theta & -\sin\theta \\ \sin\theta & \cos\theta \end{bmatrix} = \begin{bmatrix} \varepsilon_{11}\cos^2\theta + \varepsilon_{22}\sin^2\theta & \cos\theta\sin\theta(\varepsilon_{11} - \varepsilon_{22}) \\ \cos\theta\sin\theta(\varepsilon_{11} - \varepsilon_{22}) & \varepsilon_{11}\sin^2\theta + \varepsilon_{22}\cos^2\theta \end{bmatrix} \tag{1}$$

where superscript ' indicates variables in the local coordinate system. θ is the angle between the two coordinate systems.

Then the mechanical responses of the PVDF film need to be inputted into the piezoelectric model for calculating the output voltage. In general, the constitutive equations for the mechanical–electric field coupling effect in a piezoelectric material can be formulated as

$$\begin{aligned} S_{ij} &= s^E_{ijkl} \cdot T_{kl} + d_{kij} \cdot E_k \\ D_j &= d_{jkl} \cdot T_{kl} + e^T_{jk} \cdot E_k \end{aligned} \tag{2}$$

where S_{ij} refers to the strain. s^E_{ijkl} is the mechanical compliance measured at constant electric field (superscript E). T_{kl} refers to the stress. E_k refers to the electric field. D_j refers to the electric displacement. e^T_{jk} is the dielectric permittivity measured at constant stress (superscript T). d_{kij}, d_{jkl} are the piezoelectric strain coefficients wherein the first subscript represents the direction of the electric field, and the second and third subscripts together represent the stress direction.

For rectangular segment i, the piezoelectric film's electrodes are located exclusively in the plane that is perpendicular to the thickness direction, thus $D^i_1 = D^i_2 = 0$. When the piezoelectric film is used as a sensor to measure the mechanical strain for the output voltage, no external electric field is applied. Hence, the electric displacement D^i_3 due to the stresses $\sigma^i_1, \sigma^i_2, \sigma^i_3$ in three directions of local coordinate system can be simply obtained as

$$D^i_3 = d_{31}\sigma^i_1 + d_{33}\sigma^i_2 + d_{32}\sigma^i_3 \tag{3}$$

The ACCCs is loaded in the plane stress state, thus the out-of-plane stress is

$$\sigma_3^i = 0 \tag{4}$$

Afterwards, the generated charge on the piezoelectric film can be obtained as the superposition of the two charge generation modes: mode 31 and mode 33, as indicated in Eq. (5).

$$q_3^i = l_i w_i (d_{31}\sigma_1^i + d_{33}\sigma_2^i) \tag{5}$$

where l_i, w_i are the length and width of each rectangular segment, respectively. l_p, w_p, t_p are the length, width, and thickness of the PVDF film. The piezoelectric film is divided into n rectangular segments of equal size along both its length and width dimensions (i.e., $l_p = nl_i$, $w_p = nw_i$). The directions of length, width, and thickness of the PVDF film correspond to direction 1, direction 3, and direction 2 in the local coordinate system, respectively.

The constitution in the plane stress state can be described as

$$\begin{Bmatrix} \sigma_1^i \\ \sigma_2^i \\ \tau_{12}^i \end{Bmatrix} = \frac{E_p}{(1-\nu_p^2)} \begin{bmatrix} 1 & \nu_p & 0 \\ \nu_p & 1 & 0 \\ 0 & 0 & \frac{(1-\nu_p)}{2} \end{bmatrix} \begin{Bmatrix} \varepsilon_1^i \\ \varepsilon_2^i \\ \gamma_{12}^i \end{Bmatrix} \tag{6}$$

where E_p, ν_p refer to the elastic modulus and Poisson's ratio of the PVDF film, respectively. τ_{12}^i is in-plane shear stress in local coordinate system. $\varepsilon_1^i, \varepsilon_2^i$ are the in-plane strains in the two direction of local coordinate system. γ_{12}^i is in-plane shear strain in local coordinate system.

Thus, with the combination of Eq. (6), Eq. (5) can be formulated as

$$q_3^i = l_i w_i \left(d_{31}\frac{E_p}{(1-\nu_p^2)}(\varepsilon_1^i + \nu_p\varepsilon_2^i) + d_{33}\frac{E_p}{(1-\nu_p^2)}(\nu_p\varepsilon_1^i + \varepsilon_2^i)\right) \tag{7}$$

The capacitance C_i of each rectangular segment can be calculated as

$$C_i = \frac{e_{33} l_i w_i}{t_p} \tag{8}$$

where t_p is the thickness of the piezoelectric layer in the PVDF film. e_{33} refers to the dielectric constant in the 2 direction of the PVDF film. Correspondingly, the capacitance C_p of the PVDF film can be represented as

$$C_p = \frac{e_{33} l_p w_p}{t_p} = n^2 C_i \tag{9}$$

The charges q_p on the electrodes of the PVDF film can be obtained by summing up the charges for each segment using Eq. (10).

$$q_p = \sum_{i=1}^{n} q_i = \frac{V_p C_p}{n} \tag{10}$$

where V_p is the total voltage of the PVDF film, which consistent across all segments.

Therefore, V_p can be expressed as the sum of two voltage components due to mode 31 and mode 33, respectively.

$$V_p = V_{p,1} + V_{p,2} \tag{11}$$

$$V_{p,1} = \frac{l_p w_p d_{31}}{C_p}\frac{E_p}{n(1-\nu_p^2)}\sum_{i=1}^{n}(\varepsilon_1^i + \nu_p\varepsilon_1^i) = \frac{l_p w_p d_{31}}{C_p}\frac{1}{n}\sum_{i=1}^{n}\sigma_1^{'} = \frac{l_p w_p d_{31}}{C_p}\overline{\sigma}_1^{'} \tag{12}$$

$$V_{p,2} = \frac{l_p w_p d_{33}}{C_p}\frac{E_p}{n(1-\nu_p^2)}\sum_{i=1}^{n}(\nu_p\varepsilon_1^i + \varepsilon_2^i) = \frac{l_p w_p d_{33}}{C_p}\frac{1}{n}\sum_{i=1}^{n}\sigma_2^{'} = \frac{l_p w_p d_{33}}{C_p}\overline{\sigma}_2^{'} \tag{13}$$

wherein $\overline{\sigma}_1^{'}$ is defined as the equivalent d_{31}-directional stress for the PVDF film. $\overline{\sigma}_2^{'}$ is the equivalent d_{33}-directional stress for the PVDF film. $V_{p,1}$ is defined as the cumulative voltage induced by $\overline{\sigma}_1^{'}$. $V_{p,2}$ is the cumulative voltage induced by $\overline{\sigma}_2^{'}$.

Therefore, the mechanical responses calculated in the local coordinate system were inputted into the analytical formulas of the piezoelectric model to obtain the output voltage. It is noteworthy that the analytical formulas for piezoelectric model can calculate the voltage components and corresponding stress components under two charge generation modes of d_{31} and d_{33}. Table 6 gives the piezoelectric properties and mechanical properties of the PVDF film used in the piezoelectric model. Wherein ρ_p refers to the density of the PVDF film. f_{eu} is the yield strength of the PVDF film. k_{31} is the electromechanical coupling factor of the PVDF film.

4. Modelling results and discussion

As displayed in Fig. 13, the simulated results based on the energy harvesting model of the ACCCs-PVDF system presented a great agreement with the experimental measurements regarding four loading cycles, confirming the validity of our model. The oscillations in the model results occurred due to the detachment between the loading plate and ACCCs per loading cycle. Fig. 13 also shows that the energy harvesting model can account for the effects of loading amplitude and frequency on the output voltage. When subjected to the same loading amplitude, the output voltage reduces as the loading frequency increases. This is because the increase of loading frequency causes a higher acceleration for the movement of the ACCCs relative to the PVDF film, which results in reduced contact between the PVDF film and the auxetic specimen surface. Hence, less friction from the greater loading frequency leads to a lower voltage, which was reflected in the energy harvesting model with a lower friction coefficient along the tangential direction regarding the interaction between the PVDF film and ACCCs surface, as listed in Table 7.

Furthermore, as the loading amplitude increases, the harvested voltage increases accordingly. In comparison, the effects of loading amplitude on the output voltage are more significant than those of loading frequency. The reason is that the ACCCs-PVDF system exhibits increased strain energy and greater flexural deformation in response to a higher loading amplitude. In addition, the increased flexural deformation of the ACCCs-PVDF system results in a more curved contact surface between the two. This curved surface significantly impedes the sliding of the PVDF film, leading to an increase in frictional forces, as explained in **Appendix C**. Correspondingly, the models subjected to a larger loading amplitude exhibit higher friction coefficients, as demonstrated in Table 7.

The energy harvesting model allows for the calculation of voltage components induced by the two charge generation modes of d_{31} and d_{33}, as well as their corresponding stresses under varying loading amplitudes and frequencies. Figs. 14 and 15 display these results. The total voltage of the PVDF film is the algebraic sum of the voltage components generated by d_{31} and d_{33}. Since the signs of d_{31} and d_{33} in a PVDF film are opposite, the voltages generated by d_{31} and d_{33} will be of opposite polarity in the stress scenario being studied here. $\sigma_1(d_{31})$ represents the equivalent d_{31}-directional stress $\overline{\sigma}_1$ (i.e., the equivalent tangential stress) for the PVDF film; $\sigma_2(d_{33})$ represents the equivalent d_{33}-directional stress $\overline{\sigma}_2$ (i.e., the equivalent normal stress) for the PVDF film. The equivalent d_{31}-directional stress $\overline{\sigma}_1$ is larger than the d_{33}-directional stress $\overline{\sigma}_2$ during per cycle for energy harvesting. Correspondingly, the output voltage $V_{p,1}$ generated by d_{31}-coupling mode is greater than the output voltage $V_{p,2}$ generated by d_{33}-coupling mode. This is because the flexural behavior of the PVDF film enables it to utilize the d_{31}-coupling mode, which results in a strong voltage generation.

The results presented in Figs. 14, 15 also illustrate the effects of loading amplitude and loading frequency on the output voltage regarding the stress components and corresponding voltage components. It can be found that $\overline{\sigma}_1$, $\overline{\sigma}_2$ under the loading amplitude of 2.0 mm are greater than those under the loading amplitude of 1.0 mm.

Correspondingly, $V_{p,1}$, $V_{p,2}$ become greater when the loading amplitude increases from 1.0 mm to 2.0 mm. However, with a constant loading amplitude, $\overline{\sigma'}_1$ decreases as the loading frequency increases from 0.3 Hz to 2.0 Hz. In contrast, $\overline{\sigma'}_2$ increases within the same frequency range. Consistent with $\overline{\sigma'}_1$, $\overline{\sigma'}_2$, $V_{p,1}$ experiences a decrease with increasing loading frequency, while $V_{p,2}$ demonstrates an increase with the increasing loading frequency under a constant loading amplitude.

5. Conclusions

A novel piezoelectric energy harvester (PEH) has been designed with ACCCs and flexible PVDF. This ACCCs-PVDF system utilizes the surface-mounted PVDF film to harvest strain energy from the second-elasticity behavior of ACCCs during cyclic loading, which was systematically and comprehensively investigated by experiments and simulations. The main conclusions can be presented as follows:

(1) The results of the energy harvesting experiments demonstrate that the ACCCs-PVDF system generates a sinusoidal output voltage with a peak voltage of several volts within each cycle of cyclic loading. At a loading frequency of 0.3 Hz and with a loading amplitude of 2.0 mm, the system can achieve a maximum output voltage of 6.4 V, indicating promising potential for supplying self-power electronics in infrastructure.

(2) The energy harvesting experiments revealed that the output voltage of the ACCCs-PVDF system increases with the loading amplitude but decreases with the loading frequency. Numerical simulations confirmed that the energy harvesting model can account for the effects of loading amplitude and frequency on the output voltage. Specifically, a higher loading frequency reduces friction between PVDF and ACCCs, resulting in lower strain transfer and voltage output. Conversely, a greater loading amplitude increases the flexural deformation of the PVDF film and friction between PVDF and ACCCs, leading to a higher output voltage.

(3) In terms of the ACCCs-PVDF system, the model results reveal its energy harvesting mechanisms with mechanical energy conversion based on two charge generation modes of d_{31} and d_{33}. The equivalent d_{31}-directional stress (i.e., the equivalent tangential stress) of the PVDF film is greater than its equivalent d_{33}-directional stress (i.e., the equivalent normal stress) during each cycle for energy harvesting. Correspondingly, the output voltage by d_{31}-coupling mode is higher than that by d_{33}-coupling mode per cycle for energy harvesting, which reflects strong energy output by d_{31}-coupling mode due to the flexural behavior of the PVDF film. As the loading amplitude increases, the stress components $\overline{\sigma'}_1$ and $\overline{\sigma'}_2$, as well as the corresponding voltage components $V_{p,1}$ and $V_{p,2}$, all increase. However, while $\overline{\sigma'}_1$ and $V_{p,1}$ decrease with increasing loading frequency, $\overline{\sigma'}_2$ and $V_{p,2}$ increase with increasing loading frequency.

(4) The energy harvesting model can reveal electromechanical mechanisms of the ACCCs-PVDF system, considering various energy harvesting parameters such as the mechanical behavior of the ACCCs, the interaction between PVDF and ACCCs, and the analytical piezoelectric model of the PVDF film. This model was validated by the measured output voltages in experiments, which can provide valuable insights for the design and optimization of architected cementitious composites that incorporate flexible piezoelectric polymers for energy harvesting applications.

CRediT authorship contribution statement

Jinbao Xie: Conceptualization, Methodology, Software, Data curation, Validation, Formal analysis, Visualization, Writing – original draft, Writing – review & editing. **Yading Xu:** Conceptualization, Methodology, Formal analysis, Visualization, Writing – review & editing. **Zhi Wan:** Visualization, Validation, Writing – review & editing. **Ali Ghaderiaram:** Visualization, Validation, Writing – review & editing. **Erik Schlangen:** Conceptualization, Methodology, Resources, Validation, Writing – review & editing, Project administration, Supervision, Funding acquisition. **Branko Šavija:** Conceptualization, Methodology, Resources, Validation, Writing – review & editing, Project administration, Supervision, Funding acquisition.

Declaration of Competing Interest

The authors declare that they have no known competing financial interests or personal relationships that could have appeared to influence the work reported in this paper.

Data availability

Data will be made available on request.

Acknowledgements

Jinbao Xie and Zhi Wan would like to acknowledge the funding supported by China Scholarship Council (CSC) under the grant CSC No. 202006260045, 201906220205. The experimental part of the study was funded by the Dutch Science Foundation (NWO) through the Open Mind Project “Auxetic Concrete Energy Harvester”, grant number 18764. Yading Xu and Branko Šavija acknowledge the financial support of the European Research Council (ERC) within the framework of the ERC Starting Grant Project “Auxetic Cementitious Composites by 3D printing (ACC-3D)”, Grant Agreement Number 101041342. Views and opinions expressed are however those of the author(s) only and do not necessarily reflect those of the European Union or the European Research Council. Neither the European Union nor the granting authority can be held responsible for them.

Appendix A

Determination of Second-elasticity model parameters for ACCCs

As demonstrated in our previous study [22,43], the unit cell specimen of ACCCs was first applied by a displacement loading from 0 % strain to 12.5% strain (the ratio of the loading displacement to the size of the specimen) during preloading; then, cyclic loading (within the range of strain from 11.25% to 13.75%, see Fig. A1a)) with a constant amplitude of 1.25% strain was applied to the unit cell specimen with frequency of 1 Hz by a sine wave. Under the loading regime above, the unit cell of ACCCs in the study [22,43] has a sample length of 20 mm with a major axis of 10 mm and a minor axis of 6 mm, which was used as the geometric entity for elucidating the second-elasticity modeling mechanism (see Fig. A2). During the cyclic loading range, the equivalent structural elastic modulus of the ACCCs is taken as 23.51 MPa by fitting our previous experimental data of stress–strain curve [22] during the strain range of cyclic loading, as shown in Fig. A1b. Based on the reconstructed model for the cyclic loading, the elastic modulus of the base material of the ACCCs in second-elasticity model is obtained as 1825 MPa through trials and errors to get a best fitting of the experimental stress–strain curve [22], as displayed in Fig. A1c. At this stage, the CDP model is unable to accurately replicate the second-elastic behavior due to the significant plastic strain experienced by the joints in the unit cell. As a result, only a minimal amount of elastic recovery strain is observed upon unloading, as dictated by the tensile constitution inputted in the CDP model. Instead, the second-elasticity during the cyclic loading test can be

simulated by second-elasticity model, which agrees well with the experimental data measured in the study [22].

Appendix B

Parametric modeling of PVDF film based on deformed ACCCs

The reconstructed ACCCs specimen for second-elasticity has been re-meshed, which induced the internal profile with a different topology information compared with the initial one. Thus, the node-order-track algorithm was used again for recoding the new topology information of the internal profile (including node coordinates and node order), as illustrated in Fig. B1a. Then, the internal profile was used to build one edge of the whole PVDF film. This edge was translated by a distance of the PVDF film thickness to obtain another edge of the PVDF film (see Fig. B1d). Fig. B1d also shows that how one segment of the PVDF film was constructed. First, the local coordinates $x_m^{'}$ of one edge of the segment with two points were calculated as

$$x_m^{'} = \beta_m^i x_i \tag{B1}$$

where superscript ' indicates variables in the local coordinate system. x_i is the coordinates in the global coordinate system. β_m^i is the Jacobian matrix for coordinates conversion, which can be written as

$$\beta_m^i = \frac{\partial x^i}{\partial x^m} = \begin{bmatrix} \cos\theta & \sin\theta \\ -\sin\theta & \cos\theta \end{bmatrix} \tag{B2}$$

Thus, Eq. (B1) can be rewritten as

$$\begin{bmatrix} x_1^{'} \\ x_2^{'} \end{bmatrix} = \begin{bmatrix} \cos\theta & \sin\theta \\ -\sin\theta & \cos\theta \end{bmatrix} \begin{bmatrix} x_1 \\ x_2 \end{bmatrix} \tag{B3}$$

Then, another edge of the segment with two points (coordinates $x_3^{'}, x_4^{'}$) can be easily obtained by translating a distance of the thickness h_p in the local coordinate system.

$$\begin{bmatrix} x_3^{'} \\ x_4^{'} \end{bmatrix} = \begin{bmatrix} x_1^{'} \\ x_2^{'} \end{bmatrix} + \begin{bmatrix} 0 \\ h_p \end{bmatrix} \tag{B4}$$

Finally, the global coordinates of another edge with two points are calculated as

$$x_i = \beta_i^m x_m^{'} = \left[\beta_m^i\right]^{-1} x_m^{'} \tag{B5}$$

Meanwhile, the inverse matrix of β_m^i can be calculated as

$$\left[\beta_m^i\right]^{-1} = \begin{bmatrix} \cos\theta & -\sin\theta \\ \sin\theta & \cos\theta \end{bmatrix} \tag{B6}$$

Hence, the global coordinates $x_5^{'}$, $x_6^{'}$ of another edge with two points are obtained by

$$\begin{bmatrix} x_5^{'} \\ x_6^{'} \end{bmatrix} = \begin{bmatrix} \cos\theta & \sin\theta \\ -\sin\theta & \cos\theta \end{bmatrix} \begin{bmatrix} x_3^{'} \\ x_4^{'} \end{bmatrix} \tag{B7}$$

Using the same procedure, each segment was treated in a similar manner and then connected to a film loop (as shown in Fig. B1d), which covered the entire internal profile. In fact, only a portion of the film loop is used to model the PVDF film, taking into account the actual sizes of the PVDF film and the bonding area between the PVDF film and the ACCCs, as illustrated in Fig. B1b.

In experiments, the internal profile of the ACCCs cracks in the middle part [22,37]. In CDP model, correspondingly, elements in the crack area have a large deformation due to large plastic strain. According to experimental observations, the middle part of PVDF film presents a circular arc above the crack area. Hence, the flatten middle part of the PVDF film needs to be modified to a transition arc by smoothing, as shown in Fig. B1c, e. Find two end points P_1, P_2 in the middle flat part, and their midpoint P_3. Then, P_4 is determined by the distance of δ_p, which is determined by experiments. The coordinates of P_0 can be calculated as the center of the circle through three points of P_1, P_2, P_4. Finally, the arc connecting P_1, P_2 can be constructed to serve as the central axis of the PVDF film along the thickness direction. The parametric construction of the PVDF film enables it to be accurately fitted to the bonding area of the ACCCs, while also facilitating easy tailoring for parametric analysis and optimization design based on factors such as the practical bonding area, as well as the dimensions of the PVDF film and ACCCs.

Appendix C

Limitations for displacement penalty method

As shown in Fig. C1a, the greater relative movement differences of the surface elements in their normal direction significantly precludes the sliding of the PVDF film along the curved specimen surface. Fig. C1b gives an explanation for this phenomenon via theoretical mechanism. Take one element as an example, when this element moves from the original position (dash box) with the normal direction of n_1 to the current position (solid box) with the normal direction of n_2. The θ_2 indicates the degree of surface curvature, which represents the angle change of the normal directions after movement. l_1, l_2 are geometric dimensions of the element. d_s is the sliding distance, which can be calculated by Eq. (C1) based on formula derivation. Fig. C1c reveals the variation of d_s versus θ_2 when θ_1 takes a value of 1° for sliding forward. This gives a clear indication that the d_s decreases significantly with the increase of θ_2, which elucidates the significant limitation for sliding distance when displacement penalty method is adopted.

$$d_s = l_1(1 - \cos\theta_1) + \frac{l_1 \sin\theta_1}{\tan\theta_2} \tag{C1}$$

Appendix D

Conversions of displacement and strain between coordinate systems

The displacement conversion (see Fig. D1a) between coordinate systems can be formulated as

$$u_m^{'} = \beta_{mu_i}^{i} \tag{D1}$$

where superscript ' indicates variables in the local coordinate system. u_i is the displacement vector in the global coordinate system. $u_m^{'}$ is the displacement vector in the local coordinate system.

Further, Eq. (D1) can be rewritten as

$$\begin{bmatrix} u_1^{'} \\ u_2^{'} \end{bmatrix} = \begin{bmatrix} \cos\theta & \sin\theta \\ -\sin\theta & \cos\theta \end{bmatrix} \begin{bmatrix} u_1 \\ u_2 \end{bmatrix} \tag{D2}$$

As schematically displayed in Fig. D1b, the strain of each rectangular segment in the global coordinate system can be converted into its equivalent strain in the local coordinate system by Eq. (D3).

$$\begin{aligned} \varepsilon_{mn}^{'} &== \left(\frac{\partial u_m^{'}}{\partial x^n} + \frac{\partial u_n^{'}}{\partial x^m}\right) \\ &= \frac{1}{2}\left(\beta_m^i \frac{\partial u_i}{\partial x^j}\frac{\partial x^j}{\partial x^n} + \beta_n^j \frac{\partial u_j}{\partial x^i}\frac{\partial x^i}{\partial x^m}\right) \\ &= \frac{1}{2}\left(\beta_m^i \frac{\partial u_i}{\partial x^j}\beta_n^j + \beta_n^j \frac{\partial u_j}{\partial x^i}\beta_m^i\right) \\ &= \frac{1}{2}\left(\frac{\partial u_i}{\partial x^j} + \frac{\partial u_j}{\partial x^i}\right)\beta_m^i \beta_n^j \\ &= \beta_m^i \beta_n^j \varepsilon_{ij} \end{aligned} \tag{D3}$$

Compared with β_m^i, β_n^j can be expressed as

$$\beta_n^j = \frac{\partial x^j}{\partial x^n} = \begin{bmatrix} \cos\theta & -\sin\theta \\ \sin\theta & \cos\theta \end{bmatrix} \tag{D4}$$

As indicated in Eq. (D4), the inverse matrix of β_m^i is equal to β_n^j.

$$\beta_n^j = \left[\beta_m^i\right]^{-1} \tag{D5}$$

Hence, the matrix form of Eq. (D3) can be expressed as

$$\begin{aligned} \left[\varepsilon_{mn}^{'}\right] &= \left[\beta_m^i\right]\left[\varepsilon_{ij}\right]\left[\beta_n^j\right] \\ &= \left[\beta_m^i\right]\left[\varepsilon_{ij}\right]\left[\beta_m^i\right]^{-1} \end{aligned} \tag{D6}$$

Therefore, Eq. (D6) can be rewritten as

$$\begin{aligned} \begin{bmatrix} \varepsilon_{11}^{'} & \varepsilon_{12}^{'} \\ \varepsilon_{21}^{'} & \varepsilon_{22}^{'} \end{bmatrix} &= \begin{bmatrix} \cos\theta & \sin\theta \\ -\sin\theta & \cos\theta \end{bmatrix} \begin{bmatrix} \varepsilon_{11} & \varepsilon_{12} \\ \varepsilon_{21} & \varepsilon_{22} \end{bmatrix} \begin{bmatrix} \cos\theta & -\sin\theta \\ \sin\theta & \cos\theta \end{bmatrix} \\ &= \begin{bmatrix} \varepsilon_{11}\cos^2\theta + \varepsilon_{22}\sin^2\theta & \cos\theta\sin\theta(\varepsilon_{11} - \varepsilon_{22}) \\ \cos\theta\sin\theta(\varepsilon_{11} - \varepsilon_{22}) & \varepsilon_{11}\sin^2\theta + \varepsilon_{22}\cos^2\theta \end{bmatrix} \end{aligned} \tag{D7}$$

References

[1] T. Fan, G. Zou, L. Yang, Nano piezoelectric/piezomagnetic energy harvester with surface effect based on thickness shear mode, Composites Part B: Engineering 74 (2015) 166–170, https://doi.org/10.1016/j.compositesb.2015.01.012.

[2] U. Yaqoob, A.S.M.I. Uddin, G.-S. Chung, Synthesis of poly(vinylidenefluoride-trifluoroethylene)-0.65Pb(Mg1/3Nb2/3)O3–0.35PbTiO3-reduced graphene oxide-composite sheet and its application to flexible energy harvesting, Composites Part B: Engineering 136 (2018) 92–100, https://doi.org/10.1016/j.compositesb.2017.09.011.

[3] E. Ghafari, F. Severgnini, S. Ghahari, Y. Feng, E.J. Lee, C. Zhang, X. Jiang, N. Lu, Thermoelectric Nanocomposite for Energy Harvesting, Multifunctional Nanocomposites for Energy and Environmental Applications, (2018) 173-202. 10.1002/9783527342501.ch8.

[4] N. Lu, I. Ferguson, III-nitrides for energy production: photovoltaic and thermoelectric applications, Semiconductor Science and Technology 28 (2013), 074023, https://doi.org/10.1088/0268-1242/28/7/074023.

[5] G. Zhu, Z.-H. Lin, Q. Jing, P. Bai, C. Pan, Y. Yang, Y. Zhou, Z.L. Wang, Toward Large-Scale energy harvesting by a Nanoparticle-Enhanced triboelectric nanogenerator, Nano Letters 13 (2013) 847–853, https://doi.org/10.1021/nl4001053.

[6] S.P. Beeby, R.N. Torah, M.J. Tudor, P. Glynne-Jones, T. O'Donnell, C.R. Saha, S. Roy, A micro electromagnetic generator for vibration energy harvesting, Journal of Micromechanics and Microengineering 17 (2007) 1257–1265, https://doi.org/10.1088/0960-1317/17/7/007.

[7] H. Xiong, L. Wang, Piezoelectric energy harvester for public roadway: on-site installation and evaluation, Applied energy 174 (2016) 101–107, https://doi.org/10.1016/j.apenergy.2016.04.031.

[8] H. Zhao, J. Yu, J. Ling, Finite element analysis of cymbal piezoelectric transducers for harvesting energy from asphalt pavement, Journal of the Ceramic Society of Japan 118 (2010) 909–915, https://doi.org/10.2109/jcersj2.118.909.

[9] C. Wang, S. Wang, Z. Gao, X. Wang, Applicability evaluation of embedded piezoelectric energy harvester applied in pavement structures, Applied energy 251 (2019), 113383, https://doi.org/10.1016/j.apenergy.2019.113383.

[10] K. Huang, H. Zhang, J. Jiang, Y. Zhang, Y. Zhou, L. Sun, Y. Zhang, The optimal design of a piezoelectric energy harvester for smart pavements, International Journal of Mechanical Sciences 232 (2022), 107609, https://doi.org/10.1016/j.ijmecsci.2022.107609.

[11] I. Jung, Y.-H. Shin, S. Kim, J.-Y. Choi, C.-Y. Kang, Flexible piezoelectric polymer-based energy harvesting system for roadway applications, Applied energy 197 (2017) 222–229, https://doi.org/10.1016/j.apenergy.2017.04.020.

[12] A. Roy Chowdhury, N. Saurabh, R. Kiran, S. Patel, Effect of porous auxetic structures on low-frequency piezoelectric energy harvesting systems: a finite

element study, Applied Physics A 128 (2021) 62, https://doi.org/10.1007/s00339-021-05199-w.
[13] M. Kashfi, P. Fakhri, B. Amini, N. Yavari, B. Rashidi, L. Kong, R. Bagherzadeh, A novel approach to determining piezoelectric properties of nanogenerators based on PVDF nanofibers using iterative finite element simulation for walking energy harvesting, Journal of Industrial Textiles 51 (2020) 531S–S553, https://doi.org/10.1177/1528083720926493.
[14] L. Mateu, F. Moll, Optimum piezoelectric bending beam structures for energy harvesting using shoe inserts, Journal of Intelligent Material Systems and structures 16 (2005) 835–845, https://doi.org/10.1177/1045389X05055280.
[15] L. Mateu, F. Moll, Appropriate charge control of the storage capacitor in a piezoelectric energy harvesting device for discontinuous load operation, Sensors and Actuators A: Physical 132 (2006) 302–310, https://doi.org/10.1016/j.sna.2006.06.061.
[16] L. Moro, D. Benasciutti, Harvested power and sensitivity analysis of vibrating shoe-mounted piezoelectric cantilevers, Smart Materials and Structures 19 (2010), 115011, https://doi.org/10.1088/0964-1726/19/11/115011.
[17] D. Vatansever, R.L. Hadimani, T. Shah, E. Siores, An investigation of energy harvesting from renewable sources with PVDF and PZT, Smart Materials and Structures 20 (2011), 055019, https://doi.org/10.1088/0964-1726/20/5/055019.
[18] Y. Wang, X. Zhu, T. Zhang, S. Bano, H. Pan, L. Qi, Z. Zhang, Y. Yuan, A renewable low-frequency acoustic energy harvesting noise barrier for high-speed railways using a helmholtz resonator and a PVDF film, Applied energy 230 (2018) 52–61, https://doi.org/10.1016/j.apenergy.2018.08.080.
[19] P. Cahill, N. Nuallain Nora Aine, N. Jackson, A. Mathewson, R. Karoumi, V. Pakrashi, Energy Harvesting from Train-Induced Response in Bridges, Journal of Bridge Engineering, 19 (2014) 04014034. 10.1061/(ASCE)BE.1943-5592.0000608.
[20] B. Zhu, J. Pan, M. Zhang, C.K.Y. Leung, Predicting the strain-hardening behaviour of polyethylene fibre reinforced engineered cementitious composites accounting for fibre-matrix interaction, Cement and Concrete Composites 134 (2022), 104770, https://doi.org/10.1016/j.cemconcomp.2022.104770.
[21] Y.-F. Su, R.R. Kotian, N. Lu, Energy harvesting potential of bendable concrete using polymer based piezoelectric generator, Composites Part B: Engineering 153 (2018) 124–129, https://doi.org/10.1016/j.compositesb.2018.07.018.
[22] Y. Xu, H. Zhang, E. Schlangen, M. Luković, B. Šavija, Cementitious cellular composites with auxetic behavior, Cement and Concrete Composites 111 (2020), 103624, https://doi.org/10.1016/j.cemconcomp.2020.103624.
[23] M. Ohno, M. Pierre, K. Imagawa, T. Ishida, Simulation and learning-driven design for architected cement-based materials, Journal of Building Engineering 65 (2023), 105768, https://doi.org/10.1016/j.jobe.2022.105768.
[24] B. Deng, A. Zareei, X. Ding, J.C. Weaver, C.H. Rycroft, K. Bertoldi, Inverse design of mechanical metamaterials with target nonlinear response via a neural accelerated evolution strategy, Advanced Materials 34 (2022) 2206238, https://doi.org/10.1002/adma.202206238.
[25] M. Moini, J. Olek, J.P. Youngblood, B. Magee, P.D. Zavattieri, Additive manufacturing and performance of architectured Cement-Based materials, Advanced materials 30 (2018) 1802123, https://doi.org/10.1002/adma.201802123.
[26] S.M. Sajadi, C.S. Tiwary, A.H. Rahmati, S.L. Eichmann, C.J. Thaemlitz, D. Salpekar, A.B. Puthirath, P.J. Boul, M.M. Rahman, A. Meiyazhagan, P.M. Ajayan, Deformation resilient cement structures using 3D-printed molds, iScience 24 (2021), 102174, https://doi.org/10.1016/j.isci.2021.102174.
[27] K.E. Evans, Auxetic polymers: a new range of materials, Endeavour 15 (1991) 170–174, https://doi.org/10.1016/0160-9327(91)90123-S.
[28] H.C. Cheng, F. Scarpa, T.H. Panzera, I. Farrow, H.-X. Peng, Shear Stiffness and Energy Absorption of Auxetic Open Cell Foams as Sandwich Cores, physica status solidi (b), 256 (2019) 1800411. 10.1002/pssb.201800411.
[29] J. Ju, J.D. Summers, Compliant hexagonal periodic lattice structures having both high shear strength and high shear strain, Materials & Design 32 (2011) 512–524, https://doi.org/10.1016/j.matdes.2010.08.029.
[30] V.L. Coenen, K.L. Alderson, Mechanisms of failure in the static indentation resistance of auxetic carbon fibre laminates, physica status solidi b-Basic, Solid State Physics 248 (2011) 66–72, https://doi.org/10.1002/pssb.201083977.
[31] L.L. Hu, M.Z. Zhou, H. Deng, Dynamic indentation of auxetic and non-auxetic honeycombs under large deformation, Composite Structures 207 (2019) 323–330, https://doi.org/10.1016/j.compstruct.2018.09.066.
[32] D. Photiou, N. Prastiti, E. Sarris, G. Constantinides, On the conical indentation response of elastic auxetic materials: Effects of poisson's ratio, contact friction and cone angle, International Journal of Solids and Structures 81 (2016) 33–42, https://doi.org/10.1016/j.ijsolstr.2015.10.020.
[33] K. Khorshidi, M. Rezaeisaray, M. Karimi, Energy harvesting using vibrating honeycomb sandwich panels with auxetic core and carbon nanotube-reinforced face sheets, International Journal of Solids and Structures 256 (2022), 111988, https://doi.org/10.1016/j.ijsolstr.2022.111988.
[34] C. Qi, A. Remennikov, L.-Z. Pei, S. Yang, Z.-H. Yu, T.D. Ngo, Impact and close-in blast response of auxetic honeycomb-cored sandwich panels: Experimental tests and numerical simulations, Composite Structures 180 (2017) 161–178, https://doi.org/10.1016/j.compstruct.2017.08.020.
[35] Y. Wang, W. Zhao, G. Zhou, Q. Gao, C. Wang, Suspension mechanical performance and vehicle ride comfort applying a novel jounce bumper based on negative poisson's ratio structure, Advances in Engineering Software 122 (2018) 1–12, https://doi.org/10.1016/j.advengsoft.2018.04.001.
[36] Y. Ma, F. Scarpa, D. Zhang, B. Zhu, L. Chen, J. Hong, A nonlinear auxetic structural vibration damper with metal rubber particles, Smart Materials and Structures 22 (2013), 084012, https://doi.org/10.1088/0964-1726/22/8/084012.
[37] Y. Xu, E. Schlangen, M. Luković, B. Šavija, Tunable mechanical behavior of auxetic cementitious cellular composites (CCCs): Experiments and simulations, Construction and Building Materials 266 (2021), 121388, https://doi.org/10.1016/j.conbuildmat.2020.121388.
[38] M. Ketabdari, E. Toraldo, M. Crispino, V. Lunkar, Evaluating the interaction between engineered materials and aircraft tyres as arresting systems in landing overrun events, Case Studies in Construction Materials 13 (2020) e00446.
[39] K. Barri, Q. Zhang, J. Kline, W. Lu, J. Luo, Z. Sun, B.E. Taylor, S.G. Sachs, L. Khazanovich, Z.L. Wang, A.H. Alavi, Multifunctional Nanogenerator-Integrated metamaterial concrete systems for smart civil infrastructure, Advanced Materials (2023) 2211027, https://doi.org/10.1002/adma.202211027.
[40] Y. Xu, B. Šavija, E. Schlangen, Compression Behaviors Of Cementitious Cellular Composites With Negative Poisson's Ratio, in: FramCos, France, 2019.
[41] J.W. Sohn, J. Jeon, S.B. Choi, An investigation on dynamic signals of MFC and PVDF sensors: Experimental work, ADVANCES IN MECHANICAL ENGINEERING (2013), https://doi.org/10.1155/2013/420345.
[42] H.-H. Huang, K.-S. Chen, Design, analysis, and experimental studies of a novel PVDF-based piezoelectric energy harvester with beating mechanisms, Sensors and Actuators A: Physical 238 (2016) 317–328, https://doi.org/10.1016/j.sna.2015.11.036.
[43] Y. Xu, Architected Cementitious Cellular Materials Towards Auxetic Behavior, Ph. D. thesis, Delft University of Technology, Delft, The Netherlands, 2021.